CALIFORNIA INSTITUTE OF TECHNOLOGY

EARTHQUAKE ENGINEERING RESEARCH LABORATORY

Performance of Viscous Damping in Inelastic Seismic Analysis of Moment-Frame Buildings

John F. Hall

Professor of Civil Engineering

Department of Mechanical and Civil Engineering

REPORT NO. EERL 2018-01

PASADENA, CALIFORNIA

MARCH 2018

UPDATED SEPTEMBER 2018

APPENDIX 8 ADDED AUGUST 2019

SUMMARY

This report investigates the performance of several viscous damping formulations in the inelastic seismic response of moment-frame buildings. The evaluation employs a detailed model of a 20-story steel structure. Damping schemes included in the study are Rayleigh, condensed Rayleigh, Wilson-Penzien, tangent Rayleigh, elastic velocity Rayleigh, and one implementation of capped damping. Caughey damping is found not to be computationally viable. Differences among the damping schemes, as quantified by amounts of plastic hinge rotations and story drifts, become noticeable once these quantities reach the 3% level. In order of least to greatest hinge rotations and story drifts that occur under lateral response to horizontal ground motion, the damping schemes rank as Rayleigh (most damping action), condensed Rayleigh, Wilson-Penzien, tangent Rayleigh and capped damping, which are about the same, and elastic velocity Rayleigh (least damping action). Performance of Rayleigh damping under vertical ground motion is discussed, including the effect of soil-structure interaction. The propensity of Rayleigh damping to generate excessive damping forces and moments during inelastic seismic analysis is explained, and a parameter is introduced that can predict the potential magnitude of the effect. A review of some literature on the role of viscous damping on the inelastic seismic response of moment frame buildings is also presented.

Arup damping is discussed in Appendix 8 (added August 2019). It gives results for the 20-story building similar to tangent Rayleigh damping.

TABLE OF CONTENTS

1. INTRODUCTION

Energy dissipation that occurs during seismic response is usually considered to arise from hysteretic action in the components of the structure and from damping. The existence of damping in an actual building has been revealed from field testing and system identification studies at low levels of vibration for which a linear model of the structure suffices [1-11]. Such damping is often quantified in terms of modal damping ratios, and typical values recommended for use in inelastic seismic analysis are on the order of 2% to 4%, with the lower end of this range appropriate for steel buildings and the higher end appropriate for reinforced concrete buildings [12]. Additional suggestions are that these values should be used with fairly complete models of structural hysteresis and should be reduced for buildings taller than 30 stories [12]. Other data suggest the estimate for steel buildings is a little low [13].

Damping mechanisms in structures are poorly understood. A list of possible damping sources includes rate dependent structural behavior, nonlinear interaction between the structural frame and nonstructural elements such as cladding and partitions, friction between sliding surfaces, cracking, and opening and closing of cracks and gaps. Inelastic soil and foundation behavior as well as radiation of energy via the ground are additional mechanisms of energy dissipation, and although they can be modelled explicitly, their effect is often included with the structural damping. It is reasonable to expect that damping sources behave differently during low level vibration as compared to strong earthquake shaking. However, knowledge about the latter is scant, and the few detailed experimental studies that have been performed [14,15] did not focus on moment-frame buildings. So, an analyst has little guidance with which to construct a damping model appropriate for strong ground motions.

Notwithstanding this lack of knowledge about damping during seismic shaking, computed damping forces and moments that reach an appreciable fraction of corresponding structural forces and moments should be treated skeptically. For example, if the peak resultant damping force acting laterally on a building during an inelastic seismic analysis reaches, say, 20% of the peak horizontal structural force acting through the first-story structural elements (base shear force), the results of the analysis should be viewed as dubious since there is no plausible damping mechanism that could produce such a large force. What is a reasonable level of damping forces and moments is a question that the analyst must ultimately answer.

That computed damping forces and moments during inelastic response can reach values that seem too large has been concluded in many studies [16-26]. Such results occur in varying degrees when damping is of the linear viscous type, i.e., included in the equation of motion by a damping matrix of constant terms that multiplies a velocity vector, such as Rayleigh damping. In an inelastic analysis, structural forces and moments are bounded by strengths of the structural members, but linear viscous damping forces and moments can increase in proportion to the

velocities without limit. Further, the yielding itself of structural members can cause velocities of the associated degrees of freedom to increase, which contributes to higher computed damping forces and moments.

The purpose of this report is to provide insight into the viscous damping forces and moments that occur during inelastic seismic analysis. The structural system considered here is a moment-frame building where yielding takes place at plastic hinges. The phenomenon of concern can occur for other structural systems as well, such as a braced frame when the braces yield or buckle, but these cases are left to future study. Types of viscous damping formulations examined in this study are Rayleigh, a modified Rayleigh in which massless rotational degrees of freedom are condensed out, Wilson-Penzien [27], Caughey [28], two versions of Rayleigh that employ the tangent stiffness matrix [26], which are therefore nonlinear, and capped damping [20,29], which is also nonlinear. Some previous papers on the subject are interpreted to provide additional insight, presented toward the end of this report to draw upon the prior discussion. Arup damping is discussed in Appendix 8 (added July 2019).

Although greatly needed, this report does not provide additional data to characterize actual damping mechanisms. The focus is entirely on understanding analytical treatments of viscous damping. Hysteretic damping is not considered, although some potential difficulties associated with this type of damping are discussed in Appendix 1.

2. BASIC CONCEPTS

The spatially discretized equation of motion for nonlinear dynamic structural analysis appears as

$$[M]\{\ddot{a}(t)\} + [C]\{\dot{a}(t)\} + \{R(t)\} = \{f(t)\}, \quad (1)$$

where $[M]$ is the mass matrix; $[C]$ is the damping matrix; t denotes time; $\{R(t)\}$ is the vector of nonlinear structural forces; $\{a(t)\}$ is the vector of nodal displacements, with an over dot denoting time differentiation; and $\{f(t)\}$ is the load vector. For seismic loading, $\{a(t)\}$ is relative to the ground and $\{f(t)\}$ contains gravity loads and other time-dependent loads involving the earthquake ground motion. For linear analysis, $\{R(t)\}$ is

$$\{R(t)\} = [K]\{a(t)\}, \quad (2)$$

where $[K]$ is the stiffness matrix. In Equation 1, the damping forces have been assumed to be linear, but this does not always have to be the case.

Implicit integration of Equation 1 over time involves time stepping, linearizing the stiffness forces, and iteration. Thus, the equation for the jth iteration in advancing from time t to time $t + \Delta t$ is

$$[M]\{\ddot{a}^{(j+1)}(t+\Delta t)\} + [C]\{\dot{a}^{(j+1)}(t+\Delta t)\} + [K_T^{(j)}]\{\Delta a^{(j)}\} = \{f(t+\Delta t)\} - \{R^{(j)}(t+\Delta t)\}, \quad (3)$$

where $\left[K_T^{(j)}\right]$ is the current tangent matrix and ${}^{(j)}(t+\Delta t)$ denotes the approximation to the value at $t+\Delta t$ obtained after $j-1$ iterations. Insertion of a time integration scheme, such as constant average acceleration, leads to

$$\left[\frac{4}{\Delta t^2}M+\frac{2}{\Delta t}C+K_T^{(j)}\right]\{\Delta a^{(j)}\}=\{f(t+\Delta t)\}-\{R^{(j)}(t+\Delta t)\}-\left[\frac{4}{\Delta t^2}M+\frac{2}{\Delta t}C\right]\{a^{(j)}(t+\Delta t)\}$$
$$+\left[\frac{4}{\Delta t^2}M+\frac{2}{\Delta t}C\right]\{a(t)\}+\left[\frac{4}{\Delta t}M+C\right]\{\dot{a}(t)\}+[M]\{\ddot{a}(t)\}. \quad (4)$$

Once Equation 4 is solved for the nodal displacement increments $\{\Delta a^{(j)}\}$, the new approximation to the solution at time $t+\Delta t$ is found as

$$\{a^{(j+1)}(t+\Delta t)\}=\{a^{(j)}(t+\Delta t)\}+\{\Delta a^{(j)}\}. \quad (5)$$

Iterations continue until convergence and then a new time step commences.

For many cases, dynamic analysis of a linear structure with damping can be carried out using modal coordinates with assigned modal damping ratios based on an assumption of viscous damping. There is no need for a damping matrix. However, an equivalent (classical) damping matrix of constant terms does exist. This damping matrix would fully couple all degrees of freedom that contain mass, and the terms of the matrix would not be recognizable as corresponding to any underlying physical damping mechanism that is realistic. But this should not be of great concern because the modal representation of viscous damping for a linear system is usually adequate because it agrees well with actual vibration data in the linear range.

For nonlinear analysis, the matrix equation of motion is typically solved directly, and a representation of damping is more difficult. Ideally, the actual damping mechanisms would be modeled as they really exist, but this is not possible given gaps in current knowledge. Instead, crude representations are used, and so the computed damping actions must be monitored to ensure they are not unreasonable according to the analyst's judgement. Several types of quantities can be employed to assess the behavior of a damping formulation. For example, the maximum rate of energy dissipation due to damping can be compared to that due to hysteretic action of the structure. The rate of energy dissipation for viscous damping is given by

$$\dot{E_D}(t)=\langle\dot{a}(\mathrm{t})\rangle\{R_D(t)\}, \quad (6)$$

where $\{R_D(t)\}$ contains the damping forces and moments. In general, any assessment of damping is more meaningful if the underlying damping mechanism is physical and realistic. This is especially true if an assessment is to include the local damping forces and moments that are produced. The attributes of being physical and realistic are desirable in any case.

Toward the goal of assessing the behavior of a damping formulation during inelastic analysis, the damping ratios corresponding to the instantaneous mode shapes and frequencies have been tracked [22, 30-32]. However, since the frequencies are constantly changing as well as the mode shapes (in the typical case of nonuniform stiffness changes), the information is hard to interpret. Therefore, this writer prefers to focus on quantities such as maximum rate of energy dissipation due to damping and the actual damping forces and moments that are generated.

To illustrate some of the points, consider Rayleigh damping used for a moment-frame model containing translational and rotational degrees of freedom. The damping matrix consists of mass and stiffness proportional parts:

$$[C_R] = \alpha_0[M] + \alpha_1[K], \quad (7)$$

where α_0 and α_1 are constants. The mass proportional term $\alpha_0[M]$ corresponds to dampers that connect the structure's degrees of freedom to the ground, which is a physical mechanism but not a realistic one. Therefore, a question arises about whether such unrealistic forces should be accepted as a source of damping. The stiffness proportional term $\alpha_1[K]$ corresponds to viscous elements in parallel with the structural beams and columns of the frame. Damping forces and moments are generated by rates of deformation of these viscous elements, which is physical and somewhat realistic. At the element level, these stiffness proportional damping forces and moments can be computed as

$$\{R_{SPD}(t)\}^e = \alpha_1[K]^e\{\dot{a}(t)\}^e, \quad (8)$$

where e denotes element quantity. An assessment of such damping forces and moments can conveniently be made by comparison to forces and moments of the associated structural elements, which are bounded by strength quantities (plastic moment, for example).

Some of the first concerns about the behavior of Rayleigh damping in inelastic seismic analysis focused on large damping moments that accompanied yielding at plastic hinge locations in moment frames [16,17]. Other work on simple shear building models that contain no rotational degrees of freedom showed that Rayleigh damping forces from both the stiffness and mass proportional terms can also attain amplitudes that seem to be too large [20]. These latter findings indicate that potential problems with Rayleigh damping may be broad based. This report deals mainly with moment frames.

3. LINEAR VISCOUS DAMPING FORMULATIONS

The following sub-sections provide insight into the behavior of various viscous damping formulations that employ constant damping matrices. Only a subset of constant $[C]$ matrices is considered here: classical damping matrices, for which the eigenvectors of the damped and undamped linear systems are the same. Typically, a damping matrix is formed with the goal that the imparted modal damping ratios ξ_i of the linear system are close to desired values for all modes whose frequencies ω_i are within a frequency range of interest bounded above by ω_{max}. This process involves specifying damping ratios $\hat{\xi}_r$ at frequencies $\hat{\omega}_r$ (or periods $\hat{T}_r$). The frequency sets ω_i and $\hat{\omega}_r$ can be the same, in which case the $\hat{\xi}_r$ values will be imparted to the ξ_i, but in general the frequency sets differ. Usually, the desired damping ratios are equal to some constant value $\hat{\xi}$, although some evidence exists for a nominal increase of ξ_i with ω_i [10]. In this report, the desired level of damping is taken to be constant.

3a. *Standard Rayleigh damping*

As mentioned above, the Rayleigh damping matrix $[C_R]$ consists of stiffness and mass proportional parts (Equation 7). For linear response, the actual damping ratio ξ_i imparted to mode i with frequency ω_i depends on the constants α_0 and α_1 as follows:

$$\xi_i = \alpha_0/2\omega_i + \omega_i\alpha_1/2, \quad (9)$$

where it is evident that damping for the higher modes essentially increases in proportion to ω_i. After selecting $\widehat{\omega}_1$, $\widehat{\omega}_2$ and $\hat{\xi}$, α_0 and α_1 are found from

$$\alpha_1 = 2\hat{\xi}/(\widehat{\omega}_1 + \widehat{\omega}_2);\ \alpha_0 = \widehat{\omega}_1\widehat{\omega}_2\,\alpha_1. \quad (10)$$

The frequency $\widehat{\omega}_1$ is usually set around the first modal frequency ω_1, and then $\widehat{\omega}_2$ could be set to a multiple of ω_1 ($3\omega_1$ to $5\omega_1$) depending on ω_{max}.

Damping moments generated by Rayleigh damping during inelastic response depend on details of beam modelling, such as whether plastic hinges are represented implicitly or explicitly, the latter with rotational springs. Several cases are shown in Figure 1 for a beam in a planar moment frame where plastic hinges are of the implicit type. If there is no mass associated with the rotational degrees of freedom, then damping moments are generated by the $\alpha_1[K]$ term only.

For the element shown in Figure 1a, for which shear deformation is included, the Rayleigh damping moments are given by

$$\begin{Bmatrix} M_{BD1}(t) \\ M_{BD2}(t) \end{Bmatrix} = \alpha_1 \frac{EI_B}{L_B(1+\Psi_B)} \begin{bmatrix} 4+\Psi_B & 2-\Psi_B \\ 2-\Psi_B & 4+\Psi_B \end{bmatrix} \begin{Bmatrix} \dot{\phi}_1(t) \\ \dot{\phi}_2(t) \end{Bmatrix}, \quad (11)$$

where B denotes beam and D indicates damping, $\Psi_B = \frac{12EI_B}{GA_{SB}L_B^2}$, E = Young's modulus, I_B = moment of inertia, L_B = element length, A_{SB} = shear area, G = shear modulus, and $\phi_i(t)$ = the rotation at node i relative to the chord of the beam. This equation applies whether plastic hinges are active or not, and it also is applicable to columns. For a beam in a frame under lateral load, which can be approximately assumed to bend in double curvature so that $\dot{\phi}_1(t) = \dot{\phi}_2(t)$, Equation 11 reduces to

$$M_{DBi}(t) = \alpha_1 \frac{6EI_B}{L_B(1+\Psi_B)} \dot{\phi}_i(t). \quad (12)$$

Thus, the only response variable is the velocity of the chord-relative end rotation of the beam. This velocity can increase upon formation of plastic hinges in a beam because it is the beam moments that resist joint rotation. The amount of speed-up depends on several parameters, but it can be above a factor of 1.6 for W30 beams attached to W14 columns (see Appendix 2), which can increase the beam damping moments significantly. Speed-up is also discussed in Reference 17.

Once plastic hinges form in the beams, the rates of bending deformation in the adjacent columns decrease, and so too will the column damping moments. Therefore, the amplified damping

moment in a beam at a node because of plastic hinging there is largely resisted by increased structural moments in the adjacent columns. To the extent that the beam damping moments are excessive, demands on columns will be overestimated and false column hinging may occur during analysis. This behavior during nonlinear response differs from that of the linear case for which the sum of beam damping moments at a node is equal and opposite to the sum of column damping moments at a node [17], assuming no rotational mass.

The maximum damping moment from Equation 12 can be compared to the plastic moment strength of the beam

$$M_{PB} = Z_B \sigma_y, \quad (13)$$

where Z_B is the plastic section modulus, and σ_y is the material yield strength. The moment ratio is defined as

$$M_{rat} = \frac{M_{DBi}}{M_{PB}} = \alpha_1 \frac{6EI_B}{L_B(1+\Psi_B)} \frac{1}{Z_B \sigma_y} \dot{\phi}_{i,max} \, . \quad (14)$$

The potential to affect column behavior can be quantified by substituting the following for M_{PB} in Equation 14: half the sum of the plastic moment strengths M_{PC} for the columns above and below for an interior column, or the unhalved sum for an exterior column.

Sometimes multi-element beams are employed to capture static loads and mass from supported secondary floor beams; see Figure 1b where third-point nodes are used. With plastic hinges active at the two ends, the constant velocity solution of the three-element beam in double curvature has zero velocities for all degrees of freedom at the two third-point nodes if the hinge behavior is perfectly plastic. This means that the damping moments generated at the two ends are given by Equation 12 with the 6 replaced by $4 + \Psi_B$, L_B replaced by $L_B/3$, and Ψ_B evaluated with $L_B/3$. Thus, the damping moments are larger than what occurs with the single beam element when the plastic hinges are active, as much as a factor of two if shear deformation is small (small Ψ_B).

The beam length L_B in Equation 12 is shorter if joints are modelled with finite dimensions and, further, if cover-plated elastic end segments are present, as shown in Figure 1c. Such an arrangement can increase damping moments at the ends of the beam (nodes 1 and 2) due to the smaller L_B and because $\dot{\phi}_i(t)$ increases due to the vertical displacements of nodes 1 and 2 as the joints rotate.

So far in this discussion, plastic hinges have been represented implicitly; however, they can also be modelled explicitly using nonlinear rotational springs. Because any rotation across the spring when the plastic hinge is not active should be small, a relatively large value is used for the initial rotational stiffness K_H of the spring. This, in turn, can lead to a very large damping moment from the stiffness proportional term of Rayleigh damping when the plastic hinge is active. Essentially, $\frac{6EI_B}{L_B(1+\Psi_B)}$ in Equation 12 is replaced by K_H. This problem has been dealt with by

omitting contributions from the rotational springs to the stiffness proportional damping term [23,33]. Such a technique is closely related to tangent Rayleigh damping discussed in Section 4 (see Appendix 3), and it should produce similar results.

Damping forces produced by the mass proportional term $\alpha_0[M]$ depend on the velocity of the translational degrees of freedom relative to the ground. Its contribution to the damping action can be comparable to that of the $\alpha_1[K]$ term, as will be demonstrated in Section 6 by examining the maximum rate of energy dissipation from damping.

3b. *Condensed Rayleigh damping*

A modification to Rayleigh damping to eliminate damping moments is possible when the rotational degrees of freedom are massless [17]. The stiffness proportional damping term is formed with the massless rotational degrees of freedom condensed out of the initial stiffness matrix. Thus,

$$[C_{CR}] = \alpha_0[M] + \alpha_1[\bar{K}], \quad (15)$$

where $[\bar{K}]$ is the condensed stiffness matrix, which has been filled with zeroes for all terms situated in a row or column corresponding to a rotational degree of freedom. The mass proportional term is unchanged, as are α_0 and α_1. With the degrees of freedom partitioned into type 1 without mass (N_1 rotational degrees of freedom) and type 2 with mass (N_2 translational degrees of freedom), $[M]$ and $[\bar{K}]$ appear as:

$$[M] = \begin{bmatrix} 0 & 0 \\ 0 & M_{22} \end{bmatrix}, \; [\bar{K}] = \begin{bmatrix} 0 & 0 \\ 0 & \bar{K}_{22} \end{bmatrix}. \quad (16)$$

Dimensions of the lower right submatrices are N_2 by N_2. This partitioning is used for notational purposes only as the original degree of freedom numbering can be retained.

For linear response, use of $[C_{CR}]$ gives the same results as the standard Rayleigh damping matrix $[C_R]$. This follows from both the condensed and original systems having the same eigenvectors, frequencies and modal damping values.

The absence of damping moments with $[C_{CR}]$ means that no amplified damping moments can occur at plastic hinges (implicit or explicit) during inelastic analysis. However, a drawback of $[C_{CR}]$ is that the elemental interpretation of the stiffness proportional part is lost because of the condensation. In fact, the condensed $[\bar{K}]$ fully couples the translational degrees of freedom. The damping forces of the $\alpha_1[\bar{K}]$ term still depend on rate of deformation, a mechanism distinct from that of the $\alpha_0[M]$ term.

The coupling present in $[\bar{K}]$ destroys the bandedness of the left-side matrix in Equation 4, entailing a computational penalty. However, some of this penalty can be mitigated by using a banded approximation to $[C_{CR}]$ on the left side of Equation 4 and then eliminating the error

through iterations, which must be done anyway because of the structural nonlinearities. This approximation to $[C_{CR}]$ can be formed by truncation, i.e., zeroing the terms of $[\overline{K}]$ outside some appropriate bandwidth. See Section 7 for further discussion.

3c. *Wilson-Penzien damping*

This damping matrix is defined as [27]

$$[C_{WP}] = [M][V]\left[\text{diag}(2\hat{\xi}\omega_i)\right][V]^T[M], \quad (17)$$

where $[V]$ contains eigenvectors of the undamped system as columns, normalized with respect to $[M]$. If $[C_{WP}]$ is used in a linear analysis, a mode will have damping $\xi_i = \hat{\xi}$ if it is included in Equation 17, or it will have zero damping if it is not included. Construction of $[C_{WP}]$ entails the expense of solving for eigenvectors and frequencies. However, the number of modes needed in Equation 17 to produce converged results for inelastic analysis may be relatively few [24] for horizontal ground motion.

The appeal of $[C_{WP}]$ is the ability to set as many modal damping ratios as desired, although the physical mechanism underlying $[C_{WP}]$ is even more obscure under inelastic response than that for $[C_{CR}]$. In addition, like $[C_{CR}]$, $[C_{WP}]$ does not produce any damping moments corresponding to rotational degrees of freedom if they are massless. This is evident from Equation 17 and the distribution of zeroes imposed by the $[M]$ matrix onto $[C_{WP}]$, which is the same as for $[C_{CR}]$.

$[C_{WP}]$ has the same non-zero pattern as $[C_{CR}]$, so the bandedness of the left-side matrix in Equation 4 is similarly destroyed. However, much of the computational penalty can be avoided [16,21] by truncating $[C_{WP}]$ at the bandwidth of $[K]$ for use on the left side of Equation 4; see Section 7.

3d. *Caughey damping*

This damping matrix is defined as [28]

$$[C_G] = [M]\sum_{m=L}^{M-1+L}\alpha_m\left[[M]^{-1}[K]\right]^m, \quad (18)$$

where the summation contains M terms (not to be confused with the damping matrix $[M]$). M is selectable and L can be negative, zero or positive. Three suggested ranges for the index m are from $1-M$ to zero, from zero to $M-1$, and from 1 to M [17 ,34]. Note that $M=1$ and $L=0$ is mass proportional damping $\alpha_0[M]$, $M=1$ and $L=1$ is stiffness proportional damping $\alpha_1[K]$, and $M=2$ and $L=0$ is Rayleigh damping $\alpha_0[M]+\alpha_1[K]$. Also, any $m>1$ term involves products with $[M]^{-1}$, so the mass matrix must be nonsingular, and any $m<0$ term involves products with $[K]^{-1}$, so the stiffness matrix must be nonsingular. Finally, the bandwidth of $[C_G]$ increases with m due to the $m>1$ terms, and the presence of any $m<0$ term causes $[C_G]$ to be a full matrix.

To determine the coefficients α_m in Equation 18, select M frequencies $\widehat{\omega}_r$ spanning up to the maximum frequency of interest ω_{max} and solve the M simultaneous equations

$$\sum_{m=L}^{M-1+L} \alpha_m \widehat{\omega}_r^{2m-1} = 2\hat{\xi} \ . \quad (19)$$

Once the α_m are determined, the actual value of the modal damping ratio ξ_i imparted to mode i with frequency ω_i can be found from

$$\xi_i = \tfrac{1}{2} \sum_{m=L}^{M-1+L} \alpha_m \omega_i^{2m-1}. \quad (20)$$

The damping values ξ_i for higher modes with frequencies ω_i above ω_{max} tend to be controlled by the last terms in the summation of Equation 20. For the range of m where L is negative or zero and the last value of m is zero, then $\alpha_0 > 0$ and $\xi_i \to 0$ from the positive side as $\omega_i \to \infty$. Thus, the damping in the higher modes will be smaller than $\hat{\xi}$. For the range of m where L equals 0 or 1 and the last value of m is odd and positive, then $\alpha_{M-1+L} > 0$ and $\xi_i \to \infty$ as $\omega_i \to \infty$. Thus, the higher modes will have large positive damping, increasing rapidly with M. For the range of m where L equals 0 or 1 and the last value of m is even and positive, then $\alpha_{M-1+L} < 0$ and $\xi_i \to -\infty$ as $\omega_i \to \infty$, so this situation should be avoided because of the negative damping.

Two recognized difficulties can arise in computing $[C_G]$. First, the set of equations in Equation 19 can be ill-conditioned to a degree that restricts the number M of terms that can be included in Equation 18. Second, the ξ_i vs. ω_i relation of Equation 20 can show wide variations depending on the choice for the $\widehat{\omega}_r$ that determines the α_m. However, recent work has shown that these two issues may be resolvable [34].

Another issue is that, for application to moment frames where the rotational masses are usually taken as zero, the terms with $m > 1$ in Equation 18 involve the inversion of a singular $[M]$. This situation was not encountered in Reference 34, which considered only a shear building that consisted of a single translational degree of freedom for each floor mass. To avoid the problem when dealing with moment frames, $[M_{22}]$ and $[\overline{K}_{22}]$ (see Equation 16) can be used in Equation 18 in place of $[M]$ and $[K]$, and the result is then expanded to include the rotational degrees of freedom by adding zeroes. Large damping will still be present for the higher modes with frequencies ω_i above ω_{max}. This situation is different than Wilson-Penzien; however, like Wilson-Penzien, no damping moments will be produced.

The moment-frame example described in Section 6 was tried with Caughey damping using four terms with $m = 0,1,2,3$. $[C_G]$ proved to be much less amenable to being approximated as a banded matrix for use on the left side of Equation 4, compared to $[C_{WP}]$ and $[C_{CR}]$, and thus Caughey damping was not computationally efficient. Also, terms of $[C_G]$ corresponding to degrees of freedom with relatively low mass and high stiffness tended to blow up in the repeated multiplications by $[M]^{-1}[K]$. An extreme example of this is the vertical degree of freedom at a column splice node, where the axial stiffness can be high (especially for a multiple-story building) and mass comes only from the column itself. However, even the tributary floor mass

for a corner column can be small enough to be problematic. Caughey damping will not be considered further in this report.

4. TANGENT RAYLEIGH DAMPING

In tangent Rayleigh damping, the forces and moments associated with the stiffness proportional damping term are expressed in terms of the current tangent stiffness matrix $[K_T]$, which is otherwise used to relate increments in displacement to increments in the structural forces and moments as

$$\{dR\} = [K_T]\{da\}\,. \quad (21)$$

With the definition

$$[C_{TR}] = \alpha_0[M] + \alpha_1[K_T], \quad (22)$$

two versions of tangent Rayleigh damping have been identified [21]: an incremental version based on

$$\{dR_D\} = [C_{TR}]\{d\dot{a}\} \quad (23)$$

and a total version based on

$$\{R_D(t)\} = [C_{TR}]\{\dot{a}(t)\}. \quad (24)$$

Here, α_0 and α_1 are computed using initial properties and kept constant, rather than updated using current properties [22,35].

Regarding the incremental version, Equation 23 defines how the damping forces and moments are updated during an analysis. However, $[C_{TR}]$ is not a proper tangent matrix for damping because it does not contain the requisite partial derivatives with respect to nodal velocities. Therefore, Equation 23 must be regarded as ad hoc, and furthermore, it can lead to nonsensical results. $\{R_D(t)\}$ updated by Equation 23 will generally not return to zero when the nodal velocities become zero at the end of an analysis [21]. In addition, the phasing between $\{R_D(t)\}$ and $\{\dot{a}(t)\}$ may become such that energy is fed into the structure rather than dissipated. For these reasons, the incremental version of tangent Rayleigh damping is not recommended by this writer.

In the total version of tangent Rayleigh damping, $[C_{TR}]$ in Equation 24 serves as a secant matrix. As a simple illustration of how this type of damping works, consider a spring of elastic stiffness k and post-yield stiffness $k/20$ stretching at a velocity v. Prior to yielding of the spring, the stiffness proportional damping force is equal to $\alpha_1 kv$; at yield the damping force suddenly drops by 95% and it remains at $\alpha_1 kv/20$ until the spring unloads. Thus, there will be discontinuities in the damping force time history, with low damping force during the spring's yield excursions. Proponents of Equation 24 believe that this behavior avoids the false duplication of dissipated energy [26], but this writer sees little reason why the rules governing a damping mechanism should be tied to the yield state of the structure, sharply reducing when and where yielding is

active. In addition, tangent stiffness damping may become negative during episodes of softening. Other justifications [36] for the use of Equation 24 have been addressed by this writer elsewhere [37]; see Appendix 4.

Experimental results, such as summarized in Reference 38, have also been cited in support of tangent Rayleigh damping [26,35]. However, previous comparisons of test results with analyses that use tangent Rayleigh damping and ones that omit damping altogether do not show convincingly that the former is better than the latter. This finding is partly due to the test specimens being bare frames without multiple sources of damping. Furthermore, older analytical models tended to use Equation 23, which may not provide consistent damping.

Recently, a physical interpretation of Equation 24 has been offered [26]. Similar to plasticity theory where strains are divided into elastic and plastic parts, the nodal displacements are expressed as

$$\{a(t)\} = \{a_{el}(t)\} + \{a_{pl}(t)\}, \quad (25)$$

where the elastic part is

$$\{a_{el}(t)\} = [K]^{-1}\{R(t)\}, \quad (26)$$

and the plastic part $\{a_{pl}(t)\}$ is the difference between the total and elastic displacements. The Rayleigh damping forces and moments are modified as

$$\{R_D(t)\} = \alpha_0[M]\{\dot{a}(t)\} + \alpha_1[K]\{\dot{a}_{el}(t)\}, \quad (27)$$

where the stiffness proportional part depends on the elastic velocities. Substitution of the rate expressions

$$\{\dot{a}_{el}(t)\} = [K]^{-1}\{\dot{R}(t)\} \quad (28)$$

from Equation 26 and

$$\{\dot{R}(t)\} = [K_T]\{\dot{a}(t)\} \quad (29)$$

from Equation 21 into Equation 27 leads to

$$\{R_D(t)\} = [\alpha_0 M + \alpha_1 K_T]\{\dot{a}(t)\}, \quad (30)$$

which is the same as Equation 22/24. However, a physical basis does not imply that a method is realistic, and there is no evidence of which this writer is aware to support the dependence of the stiffness proportional damping forces and moments on the elastic part of the nodal velocities.

A further modification is to use the elastic velocities $\{\dot{a}_{el}(t)\}$ for the mass proportional term as well, referred to as elastic velocity damping [26], which will tend to reduce the mass proportional damping forces during inelastic response. In this case,

$$[C_{EVR}] = [\alpha_0 M K^{-1} K_T + \alpha_1 K_T], \quad (31)$$

which is obtained by making the appropriate substitutions in the results above, and where EVR denotes elastic velocity Rayleigh. With Equation 31, the damping forces and moments are significantly reduced throughout the structure during inelastic response, and the rate of energy dissipation due to damping can even become zero or negative whenever the structure forms a mechanism of plastic hinges.

Implementation of tangent Rayleigh damping by simply substituting Equation 22 or 31 into Equation 4 for $[C]$ may encounter convergence problems due to the sudden changes in $[K_T]$. An alternative method is described in Reference 26. First, for Equation 22, $[C]\{\dot{a}^{(j+1)}(t+\Delta t)\}$ from Equation 3 is replaced by

$$\{R_D{}^{(j+1)}(t+\Delta t)\} = \alpha_0[M]\{\dot{a}^{(j+1)}(t+\Delta t)\} + \alpha_1\{\dot{R}^{(j+1)}(t+\Delta t)\}; \quad (32)$$

$\{\dot{R}^{(j+1)}(t+\Delta t)\}$ is expressed using a backward difference in time as

$$\{\dot{R}^{(j+1)}(t+\Delta t)\} = \tfrac{1}{\Delta t}\{R^{(j+1)}(t+\Delta t) - R(t)\}; \quad (33)$$

and $\{R^{(j+1)}(t+\Delta t)\}$ is linearized as

$$\{R^{(j+1)}(t+\Delta t)\} = \{R^{(j)}(t+\Delta t)\} + \left[K_T^{(j)}\right]\{\Delta a^{(j)}\}. \quad (34)$$

After substitution into Equation 3, the resulting version of Equation 4 corresponding to Equation 22 is

$$\begin{aligned}\left[\tfrac{4}{\Delta t^2}M + \tfrac{2}{\Delta t}C + \left(1 + \tfrac{1}{\Delta t}\alpha_1\right)K_T^{(j)}\right]\{\Delta a^{(j)}\} &= \{f(t+\Delta t)\} - \{R^{(j)}(t+\Delta t)\} \\ -\tfrac{1}{\Delta t}\alpha_1\{R^{(j)}(t+\Delta t) - R(t)\} - \left[\tfrac{4}{\Delta t^2}M + \tfrac{2}{\Delta t}C\right]\{a^{(j)}(t+\Delta t)\} \\ + \left[\tfrac{4}{\Delta t^2}M + \tfrac{2}{\Delta t}C\right]\{a(t)\} + \left[\tfrac{4}{\Delta t}M + C\right]\{\dot{a}(t)\} + [M]\{\ddot{a}(t)\}. \quad (35)\end{aligned}$$

where $[C]$ is equal to $\alpha_0[M]$. Or, for Equation 31, the result is

$$\begin{aligned}\left[\tfrac{4}{\Delta t^2}M + \left(I + \tfrac{1}{\Delta t}\alpha_0 MK^{-1} + \tfrac{1}{\Delta t}\alpha_1 I\right)K_T^{(j)}\right]\{\Delta a^{(j)}\} &= \{f(t+\Delta t)\} - \{R^{(j)}(t+\Delta t)\} \\ -\tfrac{1}{\Delta t}[\alpha_0 MK^{-1} + \alpha_1 I]\{R^{(j)}(t+\Delta t) - R(t)\} \\ +[M]\left\{-\tfrac{4}{\Delta t^2}a^{(j)}(t+\Delta t) + \tfrac{4}{\Delta t^2}a(t) + \tfrac{4}{\Delta t}\dot{a}(t) + \ddot{a}(t)\right\}, \quad (36)\end{aligned}$$

where $[I]$ is the identity matrix. To avoid dealing with $[K^{-1}]$ in the left-side matrix of Equation 36, the problem solved in Section 6 demonstrates that the product of $[K^{-1}]$ and $\left[K_T^{(j)}\right]$ on the left side can be replaced by the identity matrix $[I]$. With this replacement, Equation 36 does not have any bandwidth increase in the left-side matrix from damping; neither does Equation 35.

5. CAPPED DAMPING

One way to control excessive damping forces and moments during inelastic response is to enforce limits on these quantities [20,29]. For example, in the stiffness proportional part of Rayleigh damping, the damping moments can be capped at some fraction λ of the plastic moment of the associated beam. So, basically, the damping mechanism is given a "yield" capability.

The formulation of capped viscous damping presented in this report has the following characteristics. Mass proportional damping is omitted, the reasons being that this component of damping is unrealistic and there is also no obvious way to come up with cap values. Stiffness

proportional damping with caps is employed for axial deformation in beams and columns and for shear deformation in rectangular viscous elements bounded by adjacent columns left and right and individual beams above and below. No damping moments associated with rotational degrees of freedom are generated with this implementation of capped damping.

Damping forces can be linearized as

$$\{R_D{}^{(j+1)}(t+\Delta t)\} = \{R_D{}^{(j)}(t+\Delta t)\} + \left[C_{TP}^{(j)}\right]\{\Delta\dot{a}^{(j)}\}, \quad (37)$$

where $\left[C_{TP}^{(j)}\right]$ is the tangent form of the capped damping matrix. $\left[C_{TP}^{(j)}\right]$ is assembled with contributions $[C_{TP}^{(j)}]^e$ from the beam and column elements (axial component only) and rectangular viscous elements. Equation 37 is substituted into Equation 3 for $[C]\{\dot{a}^{(j+1)}(t+\Delta t)\}$, and $\{\Delta\dot{a}^{(j)}\}$ is replaced by

$$\{\Delta\dot{a}^{(j)}\} = -\{\dot{a}(t)\} - \{\dot{a}^{(j)}(t+\Delta t)\} + \tfrac{2}{\Delta t}\{a^{(j)}(t+\Delta t) + \Delta a^{(j)} - a(t)\}. \quad (38)$$

The result, corresponding to Equation 4, is

$$\left[\tfrac{4}{\Delta t^2}M + \tfrac{2}{\Delta t}C_{TP}^{(j)} + K_T^{(j)}\right]\{\Delta a^{(j)}\} = \{f(t+\Delta t)\} - \{R^{(j)}(t+\Delta t)\} - \{R_D{}^{(j)}(t+\Delta t)\} - \left[\tfrac{4}{\Delta t^2}M + \tfrac{2}{\Delta t}\,C_{TP}^{(j)}\right]\{a^{(j)}(t+\Delta t)\}$$
$$+\left[C_{TP}^{(j)}\right]\{\dot{a}^{(j)}(t+\Delta t)\} + \left[\tfrac{4}{\Delta t^2}M + \tfrac{2}{\Delta t}\,C_{TP}^{(j)}\right]\{a(t)\} + \left[\tfrac{4}{\Delta t}M + \,C_{TP}^{(j)}\right]\{\dot{a}(t)\} + [M]\{\ddot{a}(t)\}. \quad (39)$$

The rectangular viscous element is H by W with unit thickness, and it connects to four nodes of a frame (Figure 2). There are eight translational degrees of freedom $a_i(t)$, numbered as shown. Such elements fill the entire frame. The shear strain rate at the center of the element is given by

$$\dot{\gamma}(t) = \tfrac{1}{2}\langle\tfrac{1}{H} \quad \tfrac{-1}{W} \quad \tfrac{-1}{H} \quad \tfrac{-1}{W} \quad \tfrac{-1}{H} \quad \tfrac{1}{W} \quad \tfrac{1}{H} \quad \tfrac{1}{W}\rangle\,\{\dot{a}(t)\}^e = \langle B\rangle\{\dot{a}(t)\}^e, \quad (40)$$

where $\{\dot{a}(t)\}^e$ lists the nodal velocities $\dot{a}_i(t)$. The linear material behavior of the element is characterized by a damping shear modulus G_D so that the shear stress $\tau(t)$ at the element center equals $G_D\dot{\gamma}(t)$. Yielding occurs when $|\dot{\gamma}(t)|$ exceeds the yield shear strain rate $\dot{\gamma}_y$; in which case, $|\tau(t)|$ equals the shear yield stress τ_y (cap value). In terms of the shear stress, the element damping forces are

$$\{R_D(t)\}^e = \{B\}HW\tau(t)\,. \quad (41)$$

Elemental contributions to the tangent damping matrix are

$$[C_{TP}^{(j)}]^e = \{B\}G_{TD}^{(j)}HW\langle B\rangle, \quad (42)$$

where the tangent modulus $G_{TD}^{(j)}$ equals G_D if $|\dot{\gamma}(t)| < \dot{\gamma}_y$ or equals zero if $|\dot{\gamma}(t)| \geq \dot{\gamma}_y$.

Parameters for a rectangular viscous element can be chosen as follows. The building model is subjected to an earthquake ground motion strong enough to produce significant yielding. The peak shear force in each story, denoted by F_k for story k, is extracted from the analysis. For those stories that experience yielding, these forces should be indicative of story strength. The yield stress for each viscous element in story k is then found from

$$\tau_{y,k} = \frac{\lambda F_k}{W N_k}, \quad (43)$$

where N_k is the number of elements in story k and λ is the capping fraction. The yield shear strain rate $\dot{\gamma}_y$, assumed to apply to the entire building and which determines G_D for each element as $\tau_{y,k}/\dot{\gamma}_y$, is found by ensuring that the first mode damping ratio equals the desired value $\hat{\xi}$ under linear conditions:

$$\langle V_1 \rangle [C_P] \{V_1\} = 2\hat{\xi}\omega_1 . \quad (44)$$

Finally, the capping fraction is taken as $\lambda = 2\hat{\xi}$, based on $2\hat{\xi}$ being the ratio of damping forces to stiffness forces when a linear structure is vibrating in a mode at the resonant frequency of that mode.

A concern about capped damping as implemented here is that because it is based only on the stiffness proportional term, higher modes have more damping than desired. However, the caps themselves can mitigate this effect to some extent. Figure 3 illustrates how a capped viscous damping force $F_D(t)$ behaves during harmonic motion with increasing frequency at a given displacement amplitude X_a, approaching a frequency independent state.

6. ANALYSIS OF A 20-STORY BUILDING

The purpose of this section is to demonstrate the concepts and formulations discussed in previous sections. The building analyzed is a 20-story steel moment frame that was designed as part of the SAC project for post-Northridge criteria in Los Angeles [39]. Complex features provide a realistic test of damping models, including geometric nonlinearity, strain hardening and deterioration in plastic hinges, flexible panel zones that yield, tri-element beams to represent cover-plated ends, and mid-story column nodes at splice locations. Implicit plastic hinges are employed. See Appendix 5 for a description of the software and details of the building model, which has a fundamental period of 3.61sec.

The ground motion is also from the SAC project and was generated for Los Angeles with an exceedance probability of 2% in 50 years [40]. Two horizontal components identified as LA35 and LA36 are combined into the direction that maximizes the peak-to-peak ground velocity; see Appendix 6. Maximum values for this ground motion are 996 cm/sec^2 for acceleration, 316 cm/sec for velocity, 477 cm/sec for peak-to-peak velocity, and 121 cm for displacement. For the particular building considered here, this ground motion was the most severe from the 2% in 50 year set generated for Los Angeles. Accordingly, the ground motion had to be scaled down amplitude-wise, and a scale factor F in the range of 0.20 to 0.60 is employed.

A total of seven damping cases are considered: Rayleigh (R), condensed Rayleigh (CR), Wilson-Penzien (WP), tangent Rayleigh based on Equation 22 (TR), elastic velocity Rayleigh

based on Equation 31 (EVR), capped (P) and no damping (N). Case abbreviations are used in the figures. The damping ratio $\hat{\xi}$ is selected as 0.03 at periods $\hat{T}_1$ and $\hat{T}_2$ equal to 4 sec and 1sec, respectively, for Rayleigh, condensed Rayleigh, tangent Rayleigh and elastic velocity Rayleigh. For Wilson-Penzien, eight translational modes are included, for which $\hat{\xi} = 0.03$. For capped damping, $\hat{\xi}$ = 0.03 at T_1= 3.61sec, and λ = 0.06. The earthquake analysis to determine the story $\tau_{y,k}$ values (see Equation 43) used the LA35/LA36 motion scaled down to 40% of original amplitude, and $\dot{\gamma}_y$ was determined from Equation 44 as 6.9 cm/sec. The undamped case serves as a reference. For the damped analyses, the level $\hat{\xi} = 0.03$ seems reasonable for a 20-story steel building [13].

Results of the analyses are presented in Figures 4 to 6. Most of the yielding occurs in the form of plastic hinges in the beams of the moment frame at the sections where the cover plates stop and in the columns at ground level. Panel zone yielding is minor.

Time history plots are shown in Figure 4. The lateral displacement of the12th floor (part a) shows that a significant permanent offset occurs after 10 seconds, and so the other parts of the figure focus in on the time interval from 9 to 14 seconds: maximum absolute value of the plastic hinge rotation (part b) and damping moment (part c) among all 5th-floor beams, damping force in the 4th story of the half-building model (part d), and rate of energy dissipation by damping over the half-building model (part e). A story damping force is computed as the sum of the horizontal damping forces acting on all nodes above the floor at the base of that story. The results in Figure 4 are for the ground motion scaled amplitude-wise by F = 0.50.

As seen for the 12th-floor lateral displacement (part a of Figure 4), the amount of permanent offset depends on the damping scheme. The smallest offset occurs for Rayleigh, becoming progressively larger for condensed Rayleigh, Wilson-Penzien, capped and tangent Rayleigh, which are about the same, and finally elastic velocity Rayleigh, which is closer to the undamped case than to Rayleigh. Comparable results are seen for the plastic hinge rotations for the 5th-floor beams (part b). The peak plastic hinge rotations range from 6.4% for Rayleigh to 7.4% for elastic velocity Rayleigh to 7.9% for the undamped case.

Damping moments are generated by Rayleigh, tangent Rayleigh and elastic velocity Rayleigh, and the time histories for Rayleigh and elastic velocity Rayleigh are shown in part c of Figure 4 for 5th-floor beams, those for tangent Rayleigh and elastic velocity Rayleigh being similar. The peak Rayleigh damping moment is 282 kN-m (2497 in-k), which is 17% of the beam's plastic moment strength computed using σ_y = 317 MPa (46 ksi), i.e., M_{rat} = 0.17 (see equation 14), a high value considering $\hat{\xi}$ = 0.03. This peak occurs at 10.0 seconds during active hinge yielding. The damping moments from the two other schemes track the Rayleigh ones except during times of hinge yielding, when they drop to much lower values. As a result, the peak damping moment for tangent Rayleigh and elastic velocity Rayleigh is 77 kN-m (682 in-k) at 13.2 seconds.

As seen in part d of Figure 4, maximum values of the 4th-story damping force occur during the large yield excursion, with the largest values produced by Wilson-Penzien and condensed Rayleigh. The Rayleigh damping force is smaller because, as indicated in Section 3a, amplified damping moments are largely resisted by structural moments in the columns, which produce larger structural shear forces in the columns. Damping forces from tangent Rayleigh and Rayleigh, which share the common effect of mass proportional damping, are similar. For elastic velocity Rayleigh, the initial peak in the damping force drops off quickly due to its specific treatment of the mass proportional damping term. The flat tops of capped damping are the lowest peaks among all damping schemes during the strongest portion of the response. As seen in the figure, the caps are reached during subsequent lower but more high frequency response due to capped damping being based only on the stiffness proportional damping term.

Part e of Figure 4 shows histories of the rate of energy dissipation by damping. During the large yield excursion, Rayleigh is dissipating the most energy, followed by condensed Rayleigh, Wilson-Penzien, tangent Rayleigh, capped, and elastic velocity Rayleigh (least dissipative). The lower dissipation rate for elastic velocity Rayleigh compared to tangent Rayleigh is due mainly to the different treatment of the mass proportional damping term. Although the peak dissipation rates of elastic velocity Rayleigh and capped damping are about the same, their mechanisms and consequently their time variations are quite different. Also, as seen in the figure, the energy dissipation rate of elastic velocity Rayleigh is briefly negative.

Figure 5 presents distributions over the height of the building for peak plastic hinge rotation among the beams on each floor (part a) and the peak damping force in each story of the half-building model (part b). Results in Figure 5 are for $F = 0.50$, the same ground motion scale factor used in Figure 4.

The plastic hinge rotations in part a of Figure 5 indicate that most of the yielding occurs over the lower half of the building. The variation in amplitude among the damping formulations is similar to that in the time history plot of Figure 4b. As seen in part b of Figure 5, the peak damping forces show more differences in the lower part of the building where much of the beam plastic hinging takes place, with capped damping producing the smallest forces and Wilson-Penzien producing the largest. The peak Wilson-Penzien damping forces in the 1st and 5th stories are 11% and 16%, respectively, of the peak structural forces in those stories, high values for $\hat{\xi} = 0.03$. These ratios for capped damping are about 6%, uniform over the building height, as intended, and there is no evidence of unduly amplified damping forces due to higher mode effects in these results.

Variations in four quantities as a function of the scale factor for the LA35/LA36 ground motion are shown in Figure 6: peak plastic hinge rotation in any beam (part a), peak drift in any story (part b), ratio of peak rate of energy dissipation by damping to the peak rate of hysteretic energy

dissipation in the structural members (part c), and the same energy dissipation rate ratio but only including the mass proportional damping term (part d, Wilson-Penzien and capped damping not relevant). The ground motion scale factor F is varied from 0.20 to 0.60 in increments of 0.05.

As shown in Figure 6a, peak plastic hinge rotation increases with ground motion scale factor, with the average value of the six formulations with damping increasing from 0.6% to 10% as F varies from 0.20 to 0.60. The differences among these formulations also increase with F, becoming noticeable once the plastic hinge rotations exceed about 3%. The ratio of peak plastic hinge rotation for elastic velocity Rayleigh (highest) to that for Rayleigh (lowest) is 1.05 at $F = 0.20$, and it rises to 1.28 at $F = 0.60$. The elastic velocity Rayleigh plastic rotations are closer to those of the undamped case than to Rayleigh for $F \geq 0.35$. Results for peak story drift (part b of Figure 6) show similar trends, although the differences among the various damping formulations are not quite as large.

The ratios of peak damping to peak hysteretic energy dissipation rates (part c of Figure 6) diverge significantly as F increases. All the curves start out at high values as expected due to the relatively small rate of hysteretic dissipation at low values of F. The rate ratios for Rayleigh, condensed Rayleigh and Wilson-Penzien drop to the 14% to 16% range at $F = 0.40$ and then increase to the 20% to 29% range at $F = 0.60$. These values correspond to energy dissipation rates for damping that seem unrealistically large for $\hat{\xi} = 0.03$. This is true to a lesser extent for tangent Rayleigh, whose rate ratio increases from 11% to 14% for F between 0.40 and 0.60. However, the rate ratio for elastic velocity Rayleigh decreases throughout the entire range of F, reaching 10% at $F = 0.40$ and then 6% at $F = 0.60$, which seems reasonable for $\hat{\xi} = 0.03$. However, as noted from Figure 4e, energy dissipation due to elastic velocity Rayleigh largely disappears during structural yielding. For capped damping, the peak energy dissipation rate ratio is similar to that of elastic velocity Rayleigh, but the damping dissipation continues through yielding (Figure 4e). Finally, as can be deduced from part d of Figure 6, the contribution of the mass proportional term to the peak rate of energy dissipation due to damping is significant. Depending on the damping scheme and the value of F, the mass proportional term contributes from nearly 50% to close to 100% of the total.

The results in Figures 4 to 6 indicate that the choice of damping formulation makes a noticeable difference in a building's response when the building is excited well into the inelastic range. In terms of response quantities such as plastic hinge rotation and story drift, elastic velocity Rayleigh damping is the most conservative choice. Next conservative are tangent Rayleigh and capped damping, whose plastic hinge rotations and story drifts are similar.

Appendix 7 presents additional results of the seismic analysis of the 20-story building for the higher damping value of $\hat{\xi} = 0.05$. The purpose is to explore sensitivity to the damping ratio and to indicate, perhaps crudely, what could be expected for a reinforced concrete moment frame for

which $\hat{\xi}$ = 0.05 may be appropriate. The results in Appendix 7 appear in figures similar to Figures 4 to 6, although some of the axis ranges have been altered. With the higher damping, the spread exhibited by the various damping schemes increases. For example, with reference to Figure A10a, which corresponds to Figure 6a, the ratio of peak plastic hinge rotation for elastic velocity Rayleigh/ to that for Rayleigh is 1.09 at F = 0.20, and it rises to 1.38 at F = 0.60. These ratios are 1.05 and 1.28, respectively for $\hat{\xi}$ = 0.03.

7. COMPUTATIONAL PERFORMANCE

The choice of a damping scheme affects computational requirements. This is especially true if the damping matrix is not banded, such as for condensed Rayleigh and Wilson-Penzien. However, as mentioned earlier, for these cases much of the computational penalty can be avoided by forming a banded approximation to the damping matrix via truncation, for use on the left side of the equation of motion. A tradeoff exists between the bandwidth chosen for the damping matrix and the number of iterations per step. The original damping matrix should be used on the right side. For Wilson-Penzien, right-side vector multiplication by $[C_{WP}]$ can be done component wise by the terms of Equation 17: first by $[V]^T[M]$, then by $\left[diag(2\hat{\xi}\omega_i)\right]$, then by $[M][V]$, which is much faster than using $[C_{WP}]$ directly. No such shortcut exists for condensed Rayleigh.

The analyses reported in the previous section were run for 2500 time steps with a step size of 0.01 sec. The building model has 1722 degrees of freedom and the half bandwidth of the stiffness matrix is 76. Wilson-Penzien and condensed Rayleigh damping matrices were truncated to half bandwidths of 76 and 128, respectively, for use on the left side of the equation of motion. These values are close to optimum regarding computation time. No such truncation is needed for Rayleigh, tangent Rayleigh and elastic velocity Rayleigh. For capped damping, the actual half bandwidth of the damping matrix, equal to 120, was used. The larger half bandwidths for condensed Rayleigh and capped damping could have been reduced by 36 had mid-story nodes for column splice locations not been employed. For all analyses, the tangent stiffness matrix $\left[K_T^{(j)}\right]$ was replaced by a weighted average of the elastic stiffness matrix (10%) and the current tangent stiffness matrix (90%). For capped damping, the tangent damping matrix $\left[C_{TP}^{(j)}\right]$ was replaced by a weighted average of the initial damping matrix (10%) and the current tangent damping matrix (90%). The left-side matrix was formed and factored in every iteration of every time step for all damping schemes.

Computational parameters of the analyses appear in Table 1, and for each run include the average number of iterations per time step, the maximum number of iterations for any time step, and the CPU time. The computer employed was a Dell laptop with Intel i7-6700HQ 2.60GHz

processor, and all analyses were run under external power. The Fortran code was compiled with g77 using -O optimization. Observations are as follows: 1.) Rayleigh converged in the fewest iterations and is consequently fastest overall. 2.) Tangent Rayleigh and elastic velocity Rayleigh are next fastest as they required only a few more iterations compared to Rayleigh. 3.) Wilson-Penzien required additional iterations to account for the left-side truncation of the damping matrix, but it is still within a factor of two of Rayleigh in terms of CPU time. The solution for the eight eigenvectors and eigenvalues took only about 2 CPU seconds. 4.) Capped damping suffered from the larger half bandwidth because of the presence of column splice nodes, and so it is about three times slower than Rayleigh. 5.) Condensed Rayleigh was affected by larger half bandwidth, right side multiplications with the untruncated damping matrix, and the need for significantly more iterations. It is an order of magnitude slower than Rayleigh. 6.) Lack of convergence was not an issue for any of the schemes, although capped damping experienced a few slow-to-converge time steps.

Damping scheme	Half bandwidth	Scale factor $F = 0.20$			Scale factor $F = 0.60$		
		Average iters/step	Maximum iters/step	CPU time (sec)	Average iters/step	Maximum iters/step	CPU time (sec)
R	76	1.6	4	46	2.0	5	56
CR	128	5.6	7	607	6.1	12	651
WP	76	2.3	9	74	2.9	18	91
TR	76	1.8	9	53	2.6	19	74
EVR	76	1.8	10	51	2.7	19	74
P	120	1.8	10	97	2.8	51	152

Table 1. Computational parameters for the analyses of Section 6 at two ground motion scale factors.

8. REVIEW OF SOME LITERATURE

The literature reviewed in this section consists of quantitative studies that are concerned with the amplitude of damping forces and moments generated in inelastic analysis. Only results from simulation of time history responses of moment frames to earthquake ground motions are of interest here. For use in this section, Equation 14 is rewritten as

$$M_{rat} = \beta \dot{\phi}_{i,max}, \quad (45)$$

where $\beta = \alpha_1 K_{rot} \frac{1}{M_{PB}}$ and K_{rot} is the double-curvature rotational stiffness of the beam. The terms β and $\dot{\phi}_{i,max}$ will be used as a convenient way to compare results from different moment frames and ground motions regarding beam damping moments that are generated with Rayleigh damping. The constant β depends on properties of the building and the amount of damping, and it has units of sec/rad. As an example, consider the 20-story building from Section 6 with

Rayleigh damping ($\hat{\xi} = 0.03$) and subjected to the F = 0.50 scaled LA35/LA36 ground motion. The peak damping moment in Figure 4c for a 5th-floor beam gives M_{rat} = 0.17 as noted previously. For this beam, $\beta = 1.7$ sec/rad, and a value $\dot{\phi}_{i,max}$ = 0.10 rad/sec is obtained from the analysis. The product of these terms gives the same value for M_{rat}.

8a. *References 16,18,19,21*

The problem with Rayleigh damping generating excessive damping moments in inelastic seismic analysis of moment frames appears to have been first noted in Reference 16. In that study, several reinforced concrete frames, each two bays wide, were subject to the S16E component of the 1971 record from Pacoima Dam abutment (peaks of 1148 cm/sec^2 acceleration, 114 cm/sec velocity, 37 cm displacement); see Appendix 6. Plastic hinges were modelled implicitly with perfectly plastic moment-rotation behavior, and the analysis included finite joint size and member shear deformation. In the case of a 6-story frame using $\hat{\xi} = 0.08$ at the frequencies of the first two modes, the peak resultant Rayleigh damping moment at the interior node on the second floor was 118 kN-m, and the moment strength of each beam at this location was 137 kN-m. From this writer's analysis based on the structural details provided in Reference 41, the peak elemental damping moment for these beams is about 55 kN-m, which gives M_{rat} = 0.40. Such a large damping moment should not be surprising considering $\beta = 4.4$ sec/rad, and the very strong ground motion generated a $\dot{\phi}_{i,max}$ of about 0.09 rad/sec from this writer's analysis. The main reason why β is large is the high damping level chosen. Note also that the product of β and $\dot{\phi}_{i,max}$ gives the same value for M_{rat}. Additional results for a 12-story frame are presented in Reference 16 and the other cited references.

The explanation offered in the cited references as to why such large damping moments occur with Rayleigh damping is summarized as follows: *Mass for rotational degrees of freedom is thought to be important and so it is included in the analyses. The presence of this rotational mass creates high frequency modes, and they contribute significantly to inelastic response. Large damping moments are generated by such modes due to their high modal damping values that are imparted by Rayleigh damping.* However, in this writer's opinion, results of inelastic analysis should be insensitive as to whether mass for the rotational degrees of freedom is included or not. An appropriate amount of rotational mass is too small to cause excessive Rayleigh damping moments.

Remedies to large damping moments suggested in the cited references include the use of Wilson-Penzien damping with uniform damping in all modes (including modes associated with the rotational degrees of freedom), Rayleigh damping with the second frequency $\hat{\omega}_2$ increased so that the damping imparted to the highest of the rotational modes is below critical damping, and tangent Rayleigh damping. With uniform Wilson-Penzien damping, results of inelastic analysis should be similar if rotational mass is present and the associated modes are included in the

formulation along with the translational modes, or if rotational mass is omitted and only the translational modes are included. Damping moments will be small in the first case and zero in the second case. The suggestion to reduce Rayleigh damping moments by increasing $\widehat{\omega}_2$ is effective because α_1 is reduced (see Equation 10), which reduces β in Equation 45. Results will be similar whether rotational mass is included or not. Also, as $\widehat{\omega}_2$ is increased, Rayleigh damping approaches mass proportional damping.

A final comment has to do with the amount of mass associated with the rotational degrees of freedom in the cited references, which appears to be too large. Per Reference 41, a rotational mass is summed from contributions $\frac{1}{105} m_i L_i^3$ from the beams and columns connected to a node, where m_i is the element mass per unit length and L_i is the element length. The mass m_i includes element dead weight and, for beams, the tributary floor load. The term $\frac{1}{105} m_i L_i^3$ is the diagonal term of the consistent mass matrix corresponding to a rotational degree of freedom [42]. However, a more accurate choice is $\frac{1}{420} m_i L_i^3$, which is appropriate for double curvature bending and which should be reduced further when plastic hinging occurs. However, even the too-large values used in the cited references should be within the range where the damping moments directly resulting from rotational mass are small. This has been confirmed by this writer's analysis of the 6-story frame.

8b. *Reference 17*

This study also documented large Rayleigh damping moments in inelastic seismic analysis of a moment frame, which had four stories and two bays and was modelled without finite joint size and panel zones and without shear deformation in the elements. Yielding was confined to perfectly plastic moment-rotation behavior in beam plastic hinges (implicit type). Using $\hat{\xi} = 0.05$ at the first two modal frequencies, the beam damping moment at the top exterior node reached 85% of the beam strength at that location ($M_{rat} = 0.85$). This result was obtained with the S00E component of the 1940 El Centro ground motion (peaks of 342 cm/sec^2 acceleration, 33 cm/sec velocity and 11 cm displacement), a relatively moderate excitation (Appendix 6). The reason for such a high Rayleigh damping moment is the values used for beam stiffness and strength, giving β = 24 sec/rad as computed by this writer. From the reference, the roof beam's moment of inertia I_B is 70,200 cm^4 (1686 in^4), and its plastic moment strength M_{PB} is 20.3 kN-m (180 in-kips). For comparison, a steel W21X73 has similar I_B of 66,600 cm^4 but a much larger M_{PB} of 700 kN-m (assuming σ_y = 248 MPa). Thus, this example problem is not realistic and produces greatly exaggerated damping moments relative to a beam's strength.

An argument is made in the reference that excessive damping moments can occur with Rayleigh damping because the associated rotational degrees of freedom are massless (or have small mass). The contrast with the argument discussed above in Section 8a is noted. The point of view of this

writer is that an appropriate amount of rotational mass hardly affects the speed-up phenomenon that can contribute to amplification of damping moments; see Appendix 2 for a demonstration. Reference 17 also suggests using condensed Rayleigh damping (as discussed in Sections 3b, 6 and 7) for inelastic analysis of moment frames to eliminate damping moments.

8c. *References 22,23,33*

A simplified 5-story single-bay moment frame with explicitly modelled plastic hinges in the beams was examined in Reference 22. Rayleigh damping of 2% at the 1st and 3rd modal frequencies was used, including for the rotational springs used to model the plastic hinges. The ground motion employed was the S00E component of 1940 El Centro. In one of the cases considered, the initial stiffness of the rotational springs was set to a value high enough to limit hinge rotation during linear response, and the damping moment in the 2nd-floor beam exceeded twice the plastic moment capacity of the beam. The induced column moments led to a significantly amplified structural base shear force. Such effects, which can occur even with light damping and moderate seismic excitation, are a demonstration of the egregious problem mentioned in Section 3a that can occur when damped plastic hinges are represented explicitly. Among its recommendations, Reference 22 favors the use of tangent Rayleigh damping.

Explicitly modelled plastic hinges were also used for the moment frames examined in Reference 33. To avoid generating large damping moments in the plastic hinges, no contributions from the hinge rotational springs were included in the Rayleigh damping matrix, as mentioned in Section 3a. A plastic hinge stiffness was set at 10 times the double-curvature rotational stiffness of the elastic beam, which provided the desired rigidity without causing numerical difficulties. Adjustments were made to the stiffness and damping of the elastic beam to offset the added flexibility of the hinges. This technique was further developed in Reference 23, where some time history comparisons were presented using a 1-bay, 1-story moment frame for various damping cases with $\hat{\xi} = 0.10$. Attention was paid to increased structural moments in the columns when amplified beam damping moments occur, but insufficient structural details prevent an assessment of the results here.

8d. *Reference 43*

Results of analyses of 3 and 9-story moment frames designed for Los Angeles under the SAC project [39] are presented in terms of median responses from sets of SAC ground motions developed for this site at various exceedance probabilities. Plastic hinges were modelled implicitly with a 2% strain hardening stiffness ratio. The damping schemes employed were mass proportional, tangent stiffness proportional and tangent Rayleigh (presumably Equation 22/24). The damping level was $\hat{\xi} = 0.05$. For tangent Rayleigh, the 1st and 3rd modal frequencies were used as well as other pairs of frequencies intended to account for structural softening or to avoid

suppressing higher modes. Regarding the 9-story building subjected to the ground motions with 2% exceedance probability in 50 years, the median peak story drifts were all below 3%, yet the median ratios of peak damping force on the building to peak structural base shear reached the 15% to 17% range for two of the tangent Rayleigh schemes. The study concluded that tangent Rayleigh behaves satisfactorily, although the basis of this finding seems to be that tangent Rayleigh generally produces intermediate levels of response between mass proportional damping and tangent stiffness proportional damping.

8e. *References 24,25*

The 20-story post-Northridge moment-frame building designed for Seattle as part of the SAC project [39] was examined in the study. Cover plates on the beams were omitted from the analyses, and joints were modelled without finite dimensions and panel zones. Some building models used implicit plastic hinges (referred to as distributed plasticity) and others used rotation springs. Damping formulations included Rayleigh, tangent Rayleigh (Equation 22/24) and Wilson-Penzien. When Rayleigh damping was used for the explicit plastic hinge models, it was added to the rotational springs in one case and omitted for another. Damping level was $\hat{\xi} = 0.02$ (at 1st and 3rd modal frequencies for Rayleigh and tangent Rayleigh). A horizontal ground motion identified as SE30, which was developed by the SAC project [40] for Seattle to have a 2% exceedance probability in 50 years, was employed (peaks of 1544 cm/sec^2 acceleration, 88 cm/sec velocity, 28 cm displacement). SE30 has considerably less long-period content than the ground motion LA35/LA36 used in Section 6, even at 50% scale for the latter; see Appendix 6.

All damping schemes gave similar results except Rayleigh when damping was included for the rotational springs. In this case, the large damping moments nearly eliminated any permanent deformation in the building. A conclusion of the study was that Rayleigh damping has no intrinsic problem for inelastic response history analysis of buildings, but damping should be omitted from rotational springs used to represent plastic hinges. Despite the comparable performance of tangent Rayleigh, its use was not advised for conceptual reasons. However, as explained in Appendix 3, Rayleigh without rotational spring damping and tangent Rayleigh are closely related, and the corresponding results presented in the cited references are practically identical. Wilson-Penzien damping, for which damping moments do not occur, was also recommended.

The study's conclusions should be qualified based on the moderate level of nonlinearity exhibited by building. Peak plastic hinge rotations barely exceeded 2% at a few upper floors and were less than 1% over the lower half of the building. At these levels, the results presented in Section 6 show little difference among various damping schemes, even with $\hat{\xi} = 0.03$, which is higher than $\hat{\xi} = 0.02$ used in the cited references. In addition, this writer computes β in the range of 0.5 to 0.7 using beam properties in the upper part of the building where most of the

yielding takes place, so any amplification of Rayleigh damping moments would be expected to be fairly low.

9. OTHER RELATED TOPICS

9a. *Vertical ground motion*

Past studies have argued that the vertical component of ground motion can be important and should be included in seismic analysis of structures, including frame buildings [44,45]. The high-frequency nature of vertical ground motion is effective in exciting axial forces in columns, possibly putting splices in steel columns under tension as well as affecting the bending strength and shear strength of concrete columns. When vertical ground motion is included in seismic analysis, the damping scheme must appropriately damp the vertical motions. However, damping for vertical vibration of buildings is even less well understood than damping for lateral vibration. The reasons are that vertical modes are not generally excited in forced vibration tests, and they are difficult to identify from earthquake records. In addition, Rayleigh damping (including condensed Rayleigh, tangent Rayleigh and elastic velocity Rayleigh) does not have sufficient parameters to control the damping adequately over the wide frequency range that spans horizontal and vertical responses.

Consider the 20-story building from Section 6 for which the fundamental period of lateral vibration is 3.61s. The lowest vertical modes are a cluster of twelve (because there are twelve columns in the model) with periods around 0.18 sec and lower. With Rayleigh damping of $\hat{\xi} = 0.03$ at $\hat{T}_1 = 4.0$ sec and $\hat{T}_2 = 1.0$ sec as used in Section 6, the vertical mode damping would be at least 13% of critical. Alternatively, if $\hat{T}_1$ and $\hat{T}_2$ are chosen as 4.0 sec and 0.18 sec, respectively, then the lateral modes with intermediate periods would receive low damping.

To demonstrate the effect of damping on the potential for columns to develop axial tension, the building of Section 6 is subjected to gravity loads and the vertical component of the Tarzana ground motion (peaks of 1028 cm/sec^2 acceleration, 72 cm/sec velocity and 17 cm displacement) from the 1994 Northridge earthquake. This component is quite strong with a pseudo acceleration response spectrum value of 3.8 g in the 0.18 sec range at 3% damping (Appendix 6); even so, the response of the building is essentially linear since the horizontal component of ground motion is omitted. Two Rayleigh damping cases are considered, both with $\hat{\xi} = 0.03$: one with $\hat{T}_1 = 4.0$ sec and $\hat{T}_2 = 1.0$ sec as used in Section 6, which damps the vertical response at around 13% of critical, and the other with $\hat{T}_1 = 0.3$ sec and $\hat{T}_2 = 0.1$ sec, which damps the vertical response a little under 3% of critical. Time histories of axial force are shown in Figure 7 for an interior moment-frame column in the 2nd story where column splices are located. Tension excursions occur for both damping cases but are a factor of two lower when Rayleigh damping is based on

the lateral periods (part a) compared to the vertical periods (part b). For reference, the peak axial forces of 4.7 MN tension and 10.1 MN compression (Figure 7b) compare to an axial yield strength of this column of 23.6 MN. Because the building response is essentially linear under the vertical ground motion, condensed Rayleigh, tangent Rayleigh and elastic velocity Rayleigh exhibit results similar to those of Rayleigh damping.

Ideally, both horizontal and vertical ground motions would be applied simultaneously. In this case, to avoid the high damping of the vertical response when parameters of Rayleigh damping (including condensed Rayleigh, tangent Rayleigh and elastic velocity Rayleigh) are set using the periods of the lateral modes, contributions to stiffness proportional damping from bending deformations and to mass proportional damping from horizontal degrees of freedom can be based on lateral mode periods, and contributions to stiffness proportional damping from axial deformations and to mass proportional damping from vertical degrees of freedom can be based on vertical mode periods. This suggestion involves an approximation because lateral modes also involve some column axial deformation and vertical inertia forces.

Wilson-Penzien damping should perform satisfactorily for the vertical component of ground motion. Care should be taken to ensure that the major vertical modes, at least equal to the number of columns, are included at the desired damping level in the construction of the damping matrix. For the example problem described above, results will be similar to those in Figure 7b when $\hat{\xi} = 0.03$.

When capped damping is employed in an analysis where both horizontal and vertical ground motions are applied, the stiffness proportional damping used for axial deformation of beams and columns can be based on the predominant period of the vertical modes. With $\hat{\xi} = 0.03$ and $\hat{T}_1$ =0.18 sec, results very close to those in Figure 7b have been obtained for the example problem. With the caps set at 0.06 of the axial yield strength, no capping of the axial damping forces occurs.

9b. *Soil-structure interaction*

Damping can be contributed by soil-structure interaction during an earthquake through material damping in the soil and foundation and by energy radiation away from the building via the ground. Soil-structure interaction tends to be more significant for stiffer buildings, softer soil and stronger shaking.

Established techniques are available for modelling foundations and soil in the seismic analysis of a building [46]. The simplest is to assume that the building rests on a half space and that the base of the building translates and rotates as a rigid plane. The half space can be represented by frequency-dependent impedance functions, which in many cases can be well approximated by

constant stiffness and damping terms for each degree of freedom of the rigid base. Results are available to account for inhomogeneous properties of the ground, foundation embedment, the level of material damping of the soil, etc. Seismic loading is considered to be free-field ground motions.

When soil-structure interaction is important for a case where the building undergoes inelastic behavior, foundations and soil should always be modelled explicitly as opposed to using a fixed-base structure with an equivalent amount of damping that is larger than that of the fixed-based building. The potential for excessive damping forces and moments occurring in the building, as discussed in this report, will be less in the former case.

For flexible moment-frame buildings, such as the one considered in Section 6, the effect of soil-structure interaction on lateral vibration is generally not too important, although damping in higher modes may increase somewhat [47]. However, the much higher vertical stiffness of a building means that soil-structure interaction can significantly affect its response under vertical ground motion. To demonstrate this effect, the analysis of Section 9a using vertical ground motion is repeated with soil-structure interaction included. The basement level of the building is constrained to move as a rigid plane in the vertical direction with half-space stiffness and damping constants of 16,500 MN/m (94,300 k/in) and 920 MN-sec/m (5,300 k-sec/in), respectively. These values are computed using the graphs and formulas in Reference 48 for rectangular foundation dimensions 30.5 m by 36.6 m (100 ft by 120 ft), surface shear modulus G_0 =145 MN/m^2 (3019 k/ft^2), surface shear wave velocity v_{S0} =274 m/sec (900 ft/sec), Poisson's ratio ν = 0.3, non-dimensional frequency parameter a_0 = 2, and mid-range of the parameters accounting for increase of shear modulus with depth. No soil/foundation material damping is included. Half values of the half-space stiffness and damping constants are used for the half-building model. Rayleigh damping of $\hat{\xi} = 0.03$ at $\hat{T}_1$ =0.3 sec and $\hat{T}_2$ =0.1 sec is employed for the superstructure, as in Figure 7b. Results in Figure 7c show that the column response is reduced nearly to that of Figure 7a for which the effective damping for vertical vibration is 13% of critical. Indeed, a free vibration simulation of the building without superstructure damping but including soil-structure interaction shows a significant damping effect due to the interaction. This radiation effect would be less for shallow soil underlain by rock.

A final note is that the formulations presented in Sections 3, 4 and 5 need to be modified to include soil-structure interaction. For example, with Rayleigh damping, the soil/foundation damping terms are evaluated and added into $[C_R]$ individually and do not include the product of α_1 and the soil/foundation stiffnesses. For Wilson-Penzien, soil/foundation damping should be included in the modal damping values, which requires a separate determination. In addition, when the damping formulation employed for the building contains a mass proportional term, the building's velocities used for this term should be relative to a frame attached to the base of the building that contains the additional movement of the base due to the interaction. Then, rigid

translation and rotation of the entire building receive damping from the soil/foundation only. This feature is included for the results shown in Figure 7c.

10. CONCLUSIONS

This report has examined the performance of various viscous damping schemes when used in inelastic seismic analysis of moment-frame buildings. Following is a list of the most important conclusions.

1. This writer does not recommend Rayleigh damping for use in inelastic seismic analysis because of its potential to generate excessive damping moments and forces. Beyond debate is the egregious case where plastic hinges are modelled explicitly with stiff rotational springs that are included in the stiffness proportional damping term. For implicit plastic hinges, the effects are more benign, being less severe than indicated by some early studies but more important than concluded in a recent one; see Section 8 for a review of pertinent literature. Nevertheless, these effects are unconservative and can become noticeable regarding amount of plastic hinge rotation and story drift as the degree of inelastic behavior increases, say, for plastic hinge rotations above 3% as demonstrated in Section 6 for a 20-story moment-frame building. Details of the modelling also play a role. Greater damping moments occur for smaller distance between plastic hinge locations in beams (when finite joint dimensions are included and/or when cover-plated lengths at the ends of beams are present) or if beams are divided into multiple elements between plastic hinge locations, as discussed in Section 3a. The potential for developing excessive damping moments in a given structure can be assessed by computing a β factor; refer to Section 8 for details.

2. Condensed Rayleigh and Wilson-Penzien damping schemes eliminate damping moments, but they do not appear to be entirely effective in dealing with the excessive damping effects associated with Rayleigh damping. For the 20-story building analysis presented in Section 6, using implicit plastic hinges and 3% damping, observations includ the following. a.) The peak values of story damping force for condensed Rayleigh and Wilson-Penzien exceeded that for Rayleigh damping over the part of the building experiencing the most inelastic behavior. b.) The ratio of peak rate of energy dissipation by damping to the peak rate of energy dissipation by hysteresis of the structural members, evaluated over the entire building, was in the range of 14% to 27% for condensed Rayleigh and Wilson-Penzien when the ground motion was scaled to produce significant inelastic behavior. While less than the corresponding values for Rayleigh damping, this 14% to 27% range is quite high for 3% damping.

3. Caughey damping is not suitable for general use due to computational issues.

4. For the 20-story building analysis of Section 6 (3% damping, implicit plastic hinges), tangent Rayleigh damping and elastic velocity Rayleigh damping gave more conservative results in terms of plastic hinge rotations and story drifts, i.e. larger values of these quantities, compared to Rayleigh, condensed Rayleigh and Wilson-Penzien. For building response involving significant inelastic behavior, tangent Rayleigh damping gave results approximately midway between Rayleigh and the undamped case. Elastic velocity Rayleigh gave results closer to the undamped case. While serious questions can be raised on conceptional grounds about these two methods, some performance measures, such as the energy dissipation rate ratio, showed improvement over the other damping schemes, especially for elastic velocity Rayleigh damping. However, elastic velocity Rayleigh exhibits a marked decrease in damping action as a structure moves through a collapse mechanism, with the possibility of negative damping, so it may be overly conservative. Both tangent Rayleigh damping and elastic velocity Rayleigh damping can be implemented very efficiently, with only modest increases in computation time compared to Rayleigh damping.

5. An alternative to tangent Rayleigh damping is capped damping, a form of which is developed in this report. The main feature is a rectangular viscous element that damps inter-story and inter-bay shear strain rates without the use of damping moments as described in Section 5. Capped damping utilizes a calibration run to define the lateral strength of each story, and then the caps to the damping forces are set to the product of the story strength and twice an appropriate fraction of critical damping. For the 20-story building considered in Section 6, the plastic hinge rotations and story drifts were comparable to those obtained with tangent Rayleigh damping. Computational efficiency of capped damping is reasonable, although not as good as tangent Rayleigh damping and elastic velocity Rayleigh damping.

6. One scheme to avoid the excessive damping moments produced by Rayleigh damping is to represent plastic hinges explicitly with rotational springs and then omit the stiffness contributions of the springs when forming the stiffness proportional part of the damping matrix. As explained in Appendix 3, this process is essentially equivalent to the tangent Rayleigh approach.

7. Damping of responses to vertical ground motion deserves special attention. Rayleigh damping does not have enough range to damp both the lateral motions of a building and the higher frequency vertical ones appropriately, even in the linear case. As an approximate remedy, contributions to stiffness proportional damping from bending deformations and to mass proportional damping from horizontal degrees of freedom can be based on lateral mode periods, and contributions to stiffness proportional damping from axial deformations and to mass proportional damping from vertical degrees of freedom can be based on vertical mode periods. This procedure can also be applied to condensed Rayleigh, tangent Rayleigh and elastic velocity Rayleigh as well as to the part of capped damping associated with axial stiffness. Damping from soil-structure interaction may or may not be important, but it is more likely to affect responses to vertical ground motion. In such a case, soil-structure interaction should be modelled explicitly.

8. Excessive forces and moments from the stiffness proportional term of Rayleigh damping can be associated with any type of structural element that is initially stiff and which experiences high deformation rates after yielding or buckling. In addition to plastic hinging in moment frames, examples include panel zones in moment frames that are weaker than the adjacent beams, braces in braced frames, fuses in eccentrically braced frames, and coupling beams in shear walls. Such systems merit further study.

APPENDIX 1: HYSTERETIC DAMPING

A characteristic of hysteretic damping is that the energy dissipated per cycle is independent of frequency, which may agree better with experimental data than viscous damping. Although several versions of hysteretic damping are available, usage has been limited compared to viscous damping models. Two simple types of hysteretic damping are discussed below with reference to a single degree of freedom oscillator. A possible application could be as an inter-story shear damper in a multi-story building.

In the first form of hysteretic damping, the damper force is proportional to displacement of the mass but opposes its velocity [42, first edition only]. The damper force is given by

$$F_{H1}(t) = \alpha k X(t) \, \frac{\dot{X}(t)}{|\dot{X}(t)|} \, , \quad \text{(A1)}$$

where k is the stiffness of the oscillator spring, α is a constant, and $X(t)$ is the displacement of the mass. See Figure A1a for a plot of $F_{H1}(t)$ vs $X(t)$ (solid line) over a cycle of displacement amplitude X_a. The energy dissipated over this cycle is given by

$$E_{H1} = 2\alpha k X_a^2 \, , \quad \text{(A2)}$$

which represents the enclosed area of the $F_{H1}(t)$ vs $X(t)$ relation.

An expression for the constant α can be obtained by relating the hysteretic damper to a viscous one, with the viscous damping force given by

$$F_V(t) = 2\xi k \, \frac{1}{\omega_1} \dot{X}(t) \, , \quad \text{(A3)}$$

where ω_1 is the natural frequency of the oscillator and ξ is its fraction of critical damping. Over a cycle of harmonic motion at frequency ω_1 with displacement amplitude X_a, the energy dissipated by the viscous damper is

$$E_V = 2\pi\xi k X_a^2 \, , \quad \text{(A4)}$$

which, like E_{H1}, is proportional to X_a^2. The expression for the constant α comes from equating E_{H1} and E_V; thus, $\alpha = \pi\xi$. So, for example, $\xi = 0.03$ gives $\alpha = 0.094$. Under the stated conditions, the maximum force of the hysteretic damper exceeds that of the viscous damper by a factor of $\frac{\pi}{2}$. This factor is reflected in Figure A1a where $F_V(t)$ vs $X(t)$ (dashed line) is plotted with an enclosed area equal to that of $F_{H1}(t)$ vs $X(t)$.

This first type of hysteretic damping has some major drawbacks. The peak of $F_{H1}(t)$ occurs just as the mass is stopping, and then $F_{H1}(t)$ suddenly changes sign as the mass begins to reverse. This behavior is neither realistic nor mathematically well posed, and it can present computational difficulties. In addition, for an inelastic system, $F_{H1}(t)$ can reach unrealistically high values as yielding occurs. Further, when the mass oscillates around a permanent displacement, the damper force jumps back and forth between positive and negative values of the non-zero damper force at the permanent displacement. This behavior continues as the mass tries to come to rest. In conclusion, these problems would seem to rule out this form of hysteretic damping unless significant modifications can be made.

A possibly more promising second form of hysteretic damping is provided by a hysteretic spring that is separate and distinct from the oscillator spring. For this discussion, consider the oscillator spring to have yield displacement X_y and yield force F_y, and the damper spring to be elastic-perfectly plastic with stiffness αk, yield displacement βX_y and yield force ϕF_y. A damper force $F_{H2}(t)$ vs $X(t)$ relation is shown in Figure A1b (solid line) for a cycle of displacement amplitude X_a that exceeds βX_y. No damping occurs if X_a does not exceed βX_y. Also, the energy dissipated per cycle grows only linearly with X_a due to the upper bound on the damper force. The energy dissipated per cycle is given by

$$E_{H2} = 4\phi F_y (X_a - \beta X_y) \ , \quad \text{(A5)}$$

which is the enclosed area of the $F_{H2}(t)$ vs $X(t)$ relation.

Since $\phi = \alpha\beta$, there are two independent parameters of the damper spring to be determined. An expression involving these parameters is obtained here by equating E_{H2} to E_V from Equation A4 for a cycle of displacement amplitude $X_a = X_y$ (yield displacement of the oscillator spring). This leads to an expression for α in terms of β:

$$\alpha = \frac{\pi\xi}{2} \frac{1}{\beta(1-\beta)} \ , \quad \text{(A6)}$$

where $\beta < 1$. It is desirable to make α, β and ϕ as small as possible. The choice $\beta = 0.5$ minimizes α to the value $2\pi\xi$, which is twice what was obtained for the first hysteretic damping model. For example, $\xi = 0.03$ gives $\alpha = 0.188$, which is a significant addition to the oscillator stiffness. Also, ϕ equals $\pi\xi$ with $\beta = 0.5$, which is higher than the value of 2ξ recommended as a ratio of maximum damper force to maximum structural force for capped damping in Section 5. The choice $\beta = 0.215$ reduces ϕ to 2ξ but it increases α to 9.31ξ. The $F_{H2}(t)$ vs $X(t)$ relation plotted in Figure A1b is for $\beta = 0.5$, and $F_V(t)$ vs $X(t)$ (dashed line) is shown with an enclosed area equal to that of $F_{H2}(t)$ vs $X(t)$. The ratio of the peak damping forces in Figure A1b is $\frac{\pi}{2}$.

So, the main drawbacks of this second type of hysteretic damping are the significant increase to oscillator stiffness when the damper spring in not in a yield state and the absence of damping at low amplitudes of motion. A curvilinear $F_{H2}(t)$ vs $X(t)$ relation can provide damping at low

amplitudes, but it will be small. Such a relation is also a less efficient energy dissipater than the elastic-perfectly plastic one, which makes the selection of appropriately low values for α and ϕ even more difficult than for the elastic-perfectly plastic relation.

APPENDIX 2: SPEED-UP IN JOINT ROTATION

Shown in Figure A2 is a one-bay-wide portion of a moment frame that extends vertically to mid-levels of adjacent stories. L_C and L_B are the story height and bay width, and joint dimensions are assumed to be zero for simplicity. I_B and I_C are the moments of inertia of the beam and columns. The bay is an interior one, and so half values of I_C are used for the columns. For this analysis, plastic hinges occur only in the beam. These hinges are of the implicit type and are assumed to have perfectly plastic moment-rotation behavior.

The frame in Figure A2 is under lateral load and experiences a differential horizontal velocity of $\Delta\dot{X}$ from bottom to top that is assumed to be constant. The columns bend in double curvature with points of inflection assumed to occur at mid-story. For linear behavior before any plastic hinges form, the rotational velocity of the nodes $\dot{\phi}$, which is relative to the beam chord, can be found by structural analysis as

$$\dot{\phi} = \frac{\Delta\dot{X}}{L_C}\left(1 + \frac{L_C}{L_B}\frac{I_B}{I_C}\frac{(1+\Psi_C)}{(1+\Psi_B)}\right)^{-1} \quad \text{before hinging. (A7)}$$

After plastic hinges form in the beam, the columns rotate as rigid bodies and the rotational velocity of the joints increases to

$$\dot{\phi} = \frac{\Delta\dot{X}}{L_C} \quad \text{after hinging. (A8)}$$

The ratio of these two rotational velocities is the speed-up factor $S = 1 + \frac{L_C}{L_B}\frac{I_B}{I_C}\frac{(1+\Psi_C)}{(1+\Psi_B)}$. For example, for a W30X116 beam and W14X342 column with L_C = 3.81 m and L_B = 6.10 m, S equals 1.68. Speed-up contributes to the amplified damping moments after hinges form. An additional consideration is that $\Delta\dot{X}$ may increase as well once hinges form.

The above analysis neglects the role of damping, which may impede the speed-up of joint rotation after hinges form in the beam. Figure A3 shows the time variation of $\dot{\phi}(t)$ with damping omitted (curve 1) and included ($\hat{\xi}$ = 0.03 at periods $\hat{T}_1$ = 3 sec and $\hat{T}_2$ = 1 sec, curve 2). Parameters of the analysis are W30X116 beam, W14X342 column, L_C = 3.81 m, L_B = 6.10 m, σ_y = 317 MPa (46 ksi) and $\Delta\dot{X}$ = 0.381 m/sec. The beam does not accelerate, so the results do not depend on translational floor mass. With damping included, the speed-up is complete in about 0.04 sec, which is fast compared to the expected duration of a yield excursion. This means that the contribution of speed-up to the amplified damping moment is not moderated significantly by the presence of damping itself.

Curve 3 of Figure A3 shows the additional effect of rotational mass that is added to the two nodes. At each node, the rotational mass is computed as $\frac{1}{105} m_i L_B^3$ where m_i is taken as a full-node tributary weight of 133kN (30 kips) divided by gL_B. Despite this rotational mass being at least four times too large, as discussed in Section 8a, its effect on nodal rotational velocity is negligible, which will also be true for amplified damping moment.

APPENDIX 3: RELATION BETWEEN TWO INELASTIC MODELS WITH DIFFERENT PLASTIC HINGE REPRESENTATIONS AND DAMPING SCHEMES

Consider two inelastic models that are equivalent in the absence of damping: one uses implicit plastic hinges at the ends of the beam elements and the other uses rotational springs to represent plastic hinges that are essentially rigid in the unyielded state. Assume initially that the plastic hinges are perfectly plastic. Damping is added to both models: tangent Rayleigh (Section 4, Equation 22/24) to the first one and Rayleigh to the second one except that no damping is added to the rotational springs as discussed in Section 3a and 8c. These two models with damping are also equivalent. There is no damping action associated with the plastic hinges in either model. The implicit hinges are either rigid or have a tangent stiffness of zero during yielding, and the rotational springs are undamped. Thus, all damping action is associated with elastic deformation of the beams, which is the same for both models. Also, the mass proportional damping terms act identically in both models. In practice, small differences may result due to how solution methods for the two models are implemented. Small differences may also result if the rotational springs are not completely rigid below yield. Even so, the two inelastic models with different plastic hinge representations and different damping schemes are closely related.

Consider now that the plastic hinges are not perfectly plastic, with the two inelastic models again being equivalent in the absence of damping. If damping is added as described above, there will be some damping action associated with the implicit plastic hinges, which causes the results of the two models to differ. However, such differences are expected to be small in typical situations, so, again, the two inelastic models can be considered closely related.

APPENDIX 4: JUSTIFICATION FOR TANGENT-STIFFNESS DAMPING BY OTHERS

A tangent-stiffness damping component is mainly active in elements during loading, unloading and reloading below the yield point. Justifications for the use of the tangent stiffness as a damping mechanism have been offered [36]. These arguments are restated in italics and addressed below.

In hysteretic models, for cycles prior to initial yield that are typically modelled as linear, but which can show some hysteresis in materials such as concrete, tangent-stiffness damping can supply the missing energy dissipation without affecting the forces and moments at yield. This argument sees tangent-stiffness damping as a remedy of a defect in common hysteretic models. However, the presence of tangent-stiffness damping would not be wanted for the unloading and reloading segments of a cycle extending into the yield range because, presumably, the looping would have been calibrated to dissipate the appropriate amount of energy from structural hysteresis. Additionally, for low-amplitude cycles that take place after yielding has occurred, hysteresis is already present in stiffness degrading models due to the stiffness change as the deformation axis is crossed, so again the presence of tangent-stiffness damping would be unwanted. Thus, the addition of tangent-stiffness damping to correct a deficiency in hysteretic models before first yield can be problematic.

When foundation damping is represented by structural damping instead of being modelled explicitly, tangent-stiffness damping in the structure can capture the disappearance of foundation damping during those intervals when structural yielding causes the forces applied to the foundation to remain constant. Firstly, structural yielding generally does not cause the applied foundation forces to remain constant, including overturning moment, except in the case of a single-degree-of-freedom cantilever. Secondly, even if such forces did become constant, foundation damping would not disappear. Consider a simple foundation modelled by a spring and a dashpot subjected to a force than increases over time before levelling off. The dashpot force does not suddenly become zero when the applied force becomes constant.

Tangent-stiffness damping is appropriate to model damping arising from hysteresis and sliding of nonstructural elements because these effects are expected to be small in modern buildings or would quickly degrade at low story drifts. This seems to be an argument that damping from nonstructural elements should be bounded to fairly low values rather than it exhibit some feature that is intrinsically captured by tangent-stiffness damping.

APPENDIX 5: COMPUTER CODE AND BUILDING MODEL

The computer code is written in Fortran by this writer. Gravity loads are applied first in a static analysis followed by earthquake ground motion in a dynamic analysis. Geometric nonlinearity is included through geometric stiffness at the element level and by updating the geometry of the model based on current displacements. Equations solved are those given earlier in the text except that the tangent stiffness matrix $\left[K_T^{(j)}\right]$ in Equation 4 is replaced by a weighted sum of the elastic and tangent stiffness matrices, the weighting factors being input parameters. All damping formulations discussed in Sections 3, 4 and 5 are included. Other features of the program can be gleaned from the description of the building analyzed below.

The structure is a 20-story steel moment-frame building designed under the SAC project [39] for Los Angeles using post-Northridge criteria. All member sizes, beam cover plate data, column orientations, column splice locations and doubler plate data are given in the reference. The plan and profile of the building are shown in Figure A4, and the horizontal ground motion is applied in the short direction of the building. The computer model takes advantage of symmetry and consists of one planar moment frame and one planar gravity frame linked together at floor levels by diaphragm springs. The members of the gravity frame are appropriately scaled to represent 2½ such frames from the actual building. Gravity loads and mass are calculated from floor and roof loads of 3.50 kPa (73 psf) dead and 0.48 kPa (10 psf) live, 1.20 kPa (25 psf) cladding load on the exterior surface, plus member weight. Beam and column yield strengths are 317 MPa (46 ksi) and 372 MPa (54 ksi), respectively. The foundation is taken to be rigid except as described in Section 9b.

Beams and columns are represented by two-node cubic beam elements with implicit plastic hinge capability at the nodes [49]. Moment strength, in terms of original plastic moment strength M_P, is defined as a function of maximum historical plastic rotation as shown in Figure A5, which exhibits strain hardening followed by weakening. Hardening permits an increase in bending strength of 20% above M_P at a plastic rotation of 0.02 radians, and the softening reduces the strength to zero at a plastic rotation of 0.14 radians for beams or 0.20 radians for columns, but a lower bound of 10% M_P is enforced. In terms of hardening and strength degradation, the model approximately agrees with experimental data [50]. Strain rate effects are omitted.

Each beam of the moment frame consists of three elements: an interior inelastic one and elastic ones on the ends with 100% increase in stiffness and strength to account for cover plates. Each beam of the gravity frame consists of a rigidly connected single element with stiffness and strength reduced by 90% to reflect pinned conditions. The reduced plastic moment M_{Pred} for a column as a function of current axial force P is given by

$$M_{Pred} = M_P \cdot \text{Min}\left[1, (1 - \frac{|P|}{P_y})\frac{1}{0.85}\right], \quad \text{(A9)}$$

which is appropriate for strong axis bending and where P_y is the axial yield strength of the column section. An inter-story node exists at all column splice locations.

Panel zones at beam-to-column intersections are modelled by shear elements with finite dimensions and an elastic-plastic relation using a 10% strain hardening stiffness ratio [51]. Such joint nodes employ an extra rotational degree of freedom to include panel zone flexibility. Joint thickness accounts for the presence of doubler plates.

The complete model has 548 nodes and 1722 degrees of freedom. Nodes are numbered floor-wise progressing up the building to minimize the bandwidth, resulting in a half bandwidth of 76.

A larger half bandwidth is used to accommodate some damping schemes. The first three lateral modes of the building have periods of 3.61 sec, 1.24 sec and 0.71 sec and effective masses of 78.8%, 11.6% and 3.7%.

APPENDIX 6: GROUND MOTIONS

Time history responses are computed for two ground motions in this report, and the acceleration time histories and pseudo acceleration response spectra (3% damping) for these ground motions are shown in Figure A6. The one designated LA is from the SAC project and was generated for Los Angeles with an exceedance probability of 2% in 50 years [38]. Two horizontal components identified as LA35 and LA36 are combined into the direction that maximizes the peak-to-peak ground velocity. Maximum values for this component of ground motion are 996 cm/sec^2 for acceleration, 316 cm/sec for velocity, 477 cm/sec for peak-to-peak velocity, and 121 cm for displacement. For use in Section 6, this ground motion is scaled amplitude-wise by factors ranging from 0.2 to 0.6. The other ground motion is the vertical component from Tarzana and was recorded during the 1994 Northridge earthquake. It is denoted by TZ, and has peaks of 1028 cm/sec^2 acceleration, 72 cm/sec velocity and 17 cm displacement. This motion is used full scale in Section 9.

Three other ground motions are mentioned in the literature review of Section 8. Time histories and pseudo acceleration response spectra (3% damping) of these motions are shown in Figure A7. The one designated PD is the S16E component from Pacoima Dam and was recorded during the 1971 San Fernando earthquake. If has peak values of 1148 cm/sec^2 acceleration, 114 cm/sec velocity and 37 cm displacement. EL is the S00E component from El Centro recorded during the 1940 Imperial Valley earthquake. Peak values are 342 cm/sec^2 acceleration, 33 cm/sec velocity and 11 cm displacement. The third ground motion is a horizontal component identified as SE30 from the SAC project and was generated for Seattle with an exceedance probability of 2% in 50 years [38]. It is designated SE in Figure A7 and has maximum values of 1544 cm/sec^2 acceleration, 88 cm/sec velocity and 28 cm displacement.

The ground motions recorded during actual earthquakes can be downloaded from the COSMOS website at http://www.cosmos-eq.org/

APPENDIX 7: SEISMIC RESPONSE OF THE 20-STORY BUILDING WITH HIGHER DAMPING

The results for $\hat{\xi} = 0.05$ are presented in Figures A8 to A10, which correspond to Figures 4 to 6. See Section 6 for a description of the details of the analysis and the quantities plotted.

APPENDIX 8: ARUP DAMPING

A recent paper [52] describes a viscous damping scheme that achieves frequency independent damping over a wide frequency range. This damping method is referred to as Arup damping within this appendix since it was developed by the engineering group at the Arup company. Details of the methodology, in addition to what is described here, can be found in the cited reference.

Characteristics of Arup damping are as follows:

- The frequency range over which frequency independent damping can be attained is wider than what can be achieved with Rayleigh damping. Outside of this range, at both the low and high ends, the damping level drops off, which is opposite to the trend present in Rayleigh damping.
- An increase in stiffness with increasing frequency is produced. While this could be viewed as a drawback, arguments are presented in Reference 52 that such behavior is realistic. The merits of this argument will not be discussed further here.
- A mass proportional damping term is not employed; thus, the non-physical nature of mass-proportional damping is avoided, and rigid body motions are not damped.
- The tendency of stiffness-proportional damping to produce large damping forces during yielding, especially for stiff components, is also avoided.
- Arup damping is computationally efficient and involves no increase in bandwidth or loss of symmetry in the left-side matrix in the equation of motion. Implementation is straight forward.

A8a. *Formulation*

The notation from Reference 52 is modified to match the notation used elsewhere in this report. First, consider the derivation in Section 4 of this report (Tangent Rayleigh Damping) neglecting mass-proportional damping, specifically Equations 29 and 30, which combine to give

$$\{R_D(t)\} = \alpha_1\{\dot{R}(t)\}, \quad \text{(A10)}$$

where $\alpha_1 = 2\hat{\xi}/\widehat{\omega}_1$ from Equation 10, and $\hat{\xi}$ is the desired damping ratio. Thus, the damping forces are proportional to the time rate of change of the structural forces, and the latter can be nonlinear. In Arup damping, $\{R(t)\}$ is replaced by a set of N filtered force histories $\{R_n(t)\}$, $n = 1, N$. Thus,

$$\{R_D(t)\} = 2\hat{\xi}\sum_{n=1}^{N}\frac{\chi_n}{\omega_{cn}}\{\dot{R}_n(t)\}, \quad \text{(A11)}$$

where the χ_n are additional dimensionless parameters to be determined, and the ω_{cn} are cutoff frequencies used in the filtering process. [Compared to Reference 52, damping ratio is used here instead of damping factor, and χ_n replaces $2\alpha_n$.] The $\{R_n(t)\}$ are solutions to

$$\{R_n(t)\} + \frac{1}{\omega_{cn}}\{\dot{R}_n(t)\} = \{R(t)\}, \quad \text{(A12)}$$

each one a filtered version of $\{R(t)\}$, dependent on the cutoff frequency.

The method of selection for the parameters χ_n and ω_{cn} becomes clear after a transformation of the above to the frequency domain. Taking the Fourier transforms of the time functions in Equations A11 and A12 leads to

$$\{R_D(\omega)\} = 2\hat{\xi}\sum_{n=1}^{N}\left[\chi_n\left(\frac{\omega}{\omega_{cn}}+i\right)\phi_n\right]R(\omega), \quad \text{(A13)}$$

where $\phi_n = \frac{\omega}{\omega_{cn}}/\left(1+\frac{\omega^2}{\omega_{cn}^2}\right)$, ω is the frequency parameter and $i=\sqrt{-1}$. [There is a factor of 2 difference in the definition of ϕ_n between Reference 52 and here.] In order to have frequency independent damping at the desired damping ratio $\hat{\xi}$ over a frequency range ω_{c1} to ω_{cN}, the term $\sum_{n=1}^{N}\chi_n\phi_n$ from the imaginary part of Equation A13 should be approximately equal to one over this range. For a given set of N cutoff frequencies ω_{cn}, this can be accomplished by a least squares procedure to determine values for the N χ_n by minimizing the quantity

$$\Psi(\omega) = \int_{\omega_{c1}}^{\omega_{cN}}\left[\sum_{n=1}^{N}\chi_n\phi_n - 1\right]^2 d\omega\,. \quad \text{(A14)}$$

To keep the set of χ_n within the same order of magnitude, the cutoff frequencies should be chosen so that each ω_{cn} for $n>1$ is the same multiple of the next lower cutoff frequency. Once the χ_n are determined, the resulting damping ratio as a function of frequency is given by

$$\xi(\omega) = \hat{\xi}\sum_{n=1}^{N}\chi_n\phi_n. \quad \text{(A15)}$$

Equation A13 also reveals that the damping forces are not pure damping forces; they contain a stiffness increment, which is the real part of Equation A13. This increment, as a fraction of the static stiffness, is given as a function of frequency by

$$\gamma(\omega) = 2\hat{\xi}\sum_{n=1}^{N}\chi_n\frac{\omega}{\omega_{cn}}\phi_n. \quad \text{(A16)}$$

The increment equals zero at $\omega=0$ and increases with frequency to an upper bound of $2\hat{\xi}\sum_{n=1}^{N}\chi_n$. Although referred to as a stiffness increment, this component represents a dynamic load carrying mechanism that augments that of the structure.

Evident from the frequency domain equations, Arup damping is equivalent to N Maxwell elements in parallel. See Reference 52.

As an example, consider $N=4$ with cutoff frequencies chosen as 1, 4, 16 and 64 rad/sec. Values of χ_n are determined from the least squares procedure as 1.262, 0.935, 0.705 and 1.441 in the order from n =1 to 4. For a desired damping ratio of $\hat{\xi}=0.03$, the resulting damping $\xi(\omega)$ is plotted in Figure 11a as a function of frequency. For the same parameters, the stiffness increment $\gamma(\omega)$ is plotted in Figure 11b, the upper bound being 0.26. The vertical ordinates in Figures 11a and b are both proportional to the desired damping ratio $\hat{\xi}$, which is evident from Equations A15 and A16.

The cutoff frequencies of 1, 4, 16 and 64 rad/sec used in Figure 11 would be appropriate for an analysis of the 20-story building considered here in this report, whose first three modal periods

are 3.61, 1.24 and 0.71 sec, corresponding to frequencies of 1.74, 5.1 and 8.8 rad/sec. These three modal frequencies are marked in Figure 11 with dots. Damping ratios are close to the desired 0.03 for all three modes. The stiffness increment $\gamma(\omega)$ varies from 6.6% for the fundamental mode to 13% for the third mode.

A8b. *Numerical implementation* [1]

Equations 11 and 12 are discretized in the time domain as

$$\frac{1}{2}\{R_D(t+\Delta t)+R_D(t)\} = 2\hat{\xi}\sum_{n=1}^{N}\frac{\chi_n}{\omega_{cn}\Delta t}\{R_n(t+\Delta t)-R_n(t)\} \quad \text{(A17)}$$

and

$$\frac{1}{2}\{R_n(t+\Delta t)+R_n(t)\}+\frac{1}{\omega_{cn}\Delta t}\{R_n(t+\Delta t)-R_n(t)\} = \frac{1}{2}\{R(t+\Delta t)+R(t)\}. \quad \text{(A18)}$$

$\{R_n(t+\Delta t)\}$ is found from Equation A18 as

$$\{R_n(t+\Delta t)\} = \frac{\omega_{cn}\Delta t}{2+\omega_{cn}\Delta t}\{R(t+\Delta t)+R(t)\}+\frac{2-\omega_{cn}\Delta t}{2+\omega_{cn}\Delta t}\{R_n(t)\}, \quad \text{(A19)}$$

which is substituted into Equation A17 to get the following expression for $\{R_D(t+\Delta t)\}$:

$$\{R_D(t+\Delta t)\} = \left(4\hat{\xi}\sum_{n=1}^{N}\frac{\chi_n}{2+\omega_{cn}\Delta t}\right)\{R(t+\Delta t)+R(t)\} - 8\hat{\xi}\sum_{n=1}^{N}\frac{\chi_n}{2+\omega_{cn}\Delta t}\{R_n(t)\}-\{R_D(t)\}. \quad \text{(A20)}$$

Linearization and introduction of the iteration format give

$$\left\{R_D^{(j+1)}(t+\Delta t)\right\} = \left(4\hat{\xi}\sum_{n=1}^{N}\frac{\chi_n}{2+\omega_{cn}\Delta t}\right)\left\{R^{(j+1)}(t+\Delta t)+R(t)\right\} - 8\hat{\xi}\sum_{n=1}^{N}\frac{\chi_n}{2+\omega_{cn}\Delta t}\{R_n(t)\}-\{R_D(t)\} \quad \text{(A21)}$$

$$= \left(4\hat{\xi}\sum_{n=1}^{N}\frac{\chi_n}{2+\omega_{cn}\Delta t}\right)\left[K_T^{(j)}\right]\left\{\Delta a^{(j)}\right\}+\left\{R_D^{(j)}(t+\Delta t)\right\}, \quad \text{(A22)}$$

where $\left[K_T^{(j)}\right]$ is the tangent stiffness matrix.

The damping forces as expressed by Equation A22 replace the ones in Equation 4 to produce

$$\left[\frac{4}{\Delta t^2}M+\left(1+4\hat{\xi}\sum_{n=1}^{N}\frac{\chi_n}{2+\omega_{cn}\Delta t}\right)K_T^{(j)}\right]\left\{\Delta a^{(j)}\right\} = \{f(t+\Delta t)\}-\left\{R^{(j)}(t+\Delta t)\right\}-\left\{R_D^{(j)}(t+\Delta t)\right\} - \left[\frac{4}{\Delta t^2}M\right]\left\{a^{(j)}(t+\Delta t)\right\}+\left[\frac{4}{\Delta t^2}M\right]\{a(t)\}+\left[\frac{4}{\Delta t}M\right]\{\dot{a}(t)\}+[M]\{\ddot{a}(t)\}. \quad \text{(A23)}$$

During an iteration after the structural forces are updated to $\left\{R^{(j+1)}(t+\Delta t)\right\}$, the damping forces are updated using Equation A21 to $\left\{R_D^{(j+1)}(t+\Delta t)\right\}$. Once convergence is achieved in a time step, the filtered structural forces $\{R_n(t+\Delta t)\}$ are found from Equation A19.

When a dynamic analysis using Arup damping is applied following a static analysis, such as due to gravity loads, damping forces are initially zero. This means that when using Equation A21, $\left\{R^{(j+1)}(t+\Delta t)\right\}$, $\{R(t)\}$ and $\{R_n(t)\}$ should all initially be set to the static load vector.

[1] Y. Huang of Arup company provided direct input to this section.

A8c. *Performance*

To examine the performance of Arup damping in a simple way, a single-degree-of-freedom oscillator with period the same as the fundamental period 3.61 sec of the 20-story building (frequency of 1.74 rad/sec), is subjected to sinusoidal displacement histories at frequencies of 1.74, 5.1 and 8.8 rad/sec, the same as the frequencies of the first three modes of the 20-story building. The spring of the oscillator is elastic perfectly plastic with yield force denoted by F_y and yield displacement denoted by Δ_y. The desired damping ratio $\hat{\xi} = 0.03$ and the cutoff frequencies 1, 4, 16 and 64 rad/sec are employed. Plots of the spring force (dashed line) and the damping force at the three frequencies (solid lines) as a function of oscillator displacement are shown in Figures 12 and 13 for Arup damping (parts a), Rayleigh (parts b), tangent Rayleigh (parts c) and capped damping (parts d). For capped damping, the cap is set at $2\hat{\xi}F_y$. In Figure 12, the displacement amplitude equals the yield displacement Δ_y, in which case the spring force is linear. In Figure 13, the displacement amplitude equals four times the yield displacement ($4\Delta_y$). The plots in the figures correspond to steady-state conditions, and the spring force is independent of frequency and damping type.

For cycling at the yield displacement (Figure 12), the energy dissipated per cycle from damping (area within loop) is independent of frequency for Arup damping. With capped damping, frequency independence is approached for higher frequencies since the cap is reached earlier in the cycle. The energy dissipated per cycle for Rayleigh and tangent Rayleigh increases linearly with frequency, and their damping forces are the same because the spring does not yield. The inclination of the loops for Arup damping is due to the presence of the stiffness component, which increases with frequency as indicated in Figure 11b. However, the energy dissipated per cycle is not affected. When the excitation frequency equals the fundamental frequency of the oscillator (1.74 rad/sec), all four damping schemes dissipate the same energy per cycle.

The damping behavior is more complex when the oscillator is cycled into the yield range of the spring (Figure 13, where the displacement amplitude reaches four times the yield displacement of the spring). The results can be quantified using the ratio of energy dissipated by the damper to the energy dissipated by the spring over a cycle as the frequency increases from 1.74 rad/sec to 8.8 rad/sec. For Arup damping, this ratio goes from 12% to 18%, exhibiting some moderate frequency dependence. With capped damping, the ratio is essentially constant at 8%. Both Rayleigh and tangent Rayleigh show linear frequency dependence, with the energy dissipation ratio being much larger for Rayleigh, going from 25% to 127% compared to 5% to 25% for tangent Rayleigh. Since the bottoms of these ranges correspond to a structure vibrating in its fundamental mode, the expectation is that Arup damping would give structural responses somewhere between Rayleigh (more damped) and tangent Rayleigh and capped (less damped).

Arup damping is now considered for the same 20-story building analyzed in Section 6 of this report. Damping ratios $\hat{\xi}$ of 0.03 and 0.05 are considered, and the cutoff frequency set 1, 4, 16 and 64 rad/sec is again employed. As before, the ground motion is the combined LA35/LA36 horizontal component only with rigid foundation. This motion is scaled amplitude wise by factors F ranging from 0.2 to 0.6. The results presented are a subset of those shown in Section 6 and Appendix 7. Damping moment, damping force and rate of energy dissipation are omitted here because it is not possible to separate the stiffness and damping components of Arup damping, and so the results would not be comparable with the previous results using other types of damping. Thus, only floor displacement, story drift and plastic hinge rotation are shown below. Comparisons are made with corresponding results from Rayleigh, tangent Rayleigh and no damping. In the figures, these plots are denoted by R, TR and N, respectively, while plots using Arup damping are denoted by A.

Shown in Figure 14 are time histories using the ground motion scale factor $F = 0.5$. Part a shows the 12th-floor lateral displacement history for the no damping case and Arup damping with $\hat{\xi}$ of 0.03 and 0.05. A purpose of this plot is to examine the frequency shift due to the stiffness component of Arup damping, which is visible but not pronounced, but more so with the higher damping. Parts b ($\hat{\xi} = 0.03$) and c ($\hat{\xi} = 0.05$) of Figure 14 show plastic hinge rotation (maximum among all 5th-floor beams). Arup damping gives results that are between Rayleigh and tangent Rayleigh, and closer to tangent Rayleigh.

Figure 15 presents peak plastic hinge rotation in any beam and peak drift in any story for $\hat{\xi} =$ 0.03 in parts a and b and for $\hat{\xi} = 0.05$ in parts c and d as a function of ground motion scale factor F varied from 0.20 to 0.60 in increments of 0.05. In agreement with the previous figure, Arup damping consistently gives results that are slightly smaller (more damped) than tangent Rayleigh.

Finally, regarding computational performance for the 20-story building, Table A1 below reproduces part of Table 1 and includes results for Arup damping (labelled A) at $\hat{\xi} = 0.03$. Results are comparable to tangent Rayleigh damping.

Damping scheme	Half bandwidth	Scale factor $F = 0.20$			Scale factor $F = 0.60$		
		Average iters/step	Maximum iters/step	CPU time (sec)	Average iters/step	Maximum iters/step	CPU time (sec)
R	76	1.6	4	46	2.0	5	56
TR	76	1.8	9	53	2.6	19	74
A	76	2.0	10	58	2.6	50	72

Table A1. Computational parameters for two analyses of the 20-story building from Section 6 and for Arup damping of Appendix 8 at two ground motion scale factors.

11. REFERENCES

1. Englekirk, R. E. and Matthiesen, R. B.. Forced vibration of an eight-story reinforced concrete building. *Bulletin of the Seismological Society of America.* Vol. 57, No. 3, 1967, pp. 421-436.

2. Jennings, P. C. and Kuroiwa, J. H. Vibration and soil-structure interaction tests of a nine-story reinforced concrete building. *Bulletin of the Seismological Society of America.* Vol. 58, No. 3, 1968, pp. 891-916.

3. Jennings, P. C., Matthiesen, R. B. and Hoerner, J. B. Forced vibration of a tall steel-frame building. *Earthquake Engineering and Structural Dynamics*. Vol. 1, Issue 2, 1972, pp. 107-132.

4. Trifunac, M. Comparisons between ambient and forced vibration experiments. *Earthquake Engineering and Structural Dynamics*. Vol. 1, Issue 2, 1972, pp. 133-150.

5. Bouwkamp, J. G. and Stephen, R. M. Ambient and forced vibration studies of a multistory pyramid-shaped building. *Proceedings of the 5th World Conference on Earthquake Engineerin*g, Rome, Italy. Vol 1, 1974, pp. 260-269.

6. McVerry, G. H. *Frequency Domain Identification of Structural Models from Earthquake Records*. Report No. EERL 79-02, Earthquake Engineering Research Laboratory, California Institute of Technology, Pasadena, 1979.

7. Goel, R. K. and Chopra, A.K. *Vibration Properties of Buildings Determined from Recorded Earthquake Motions*. Report No. UCB/EERC-97/14, Earthquake Engineering Research Center, University of California, Berkeley, 1997.

8. Satake, N., Suda, K., Arakawa, T., Sasaki, A. and Tamura, Y. Damping evaluation using full-scale data of buildings in Japan. *Journal of Structural Engineering*, ASCE. Vol. 129, Issue 4, 2003, pp. 470-477.

9. Bernal, D., Döhler, M., Kojidi, S. M., Kwan, K. and Liu, Y. First mode damping ratios for buildings. *Earthquake Spectra*. Vol. 31, No. 1, 2015, pp. 367-381.

10. Cruz, C. and Miranda, E. Damping ratios in tall buildings inferred from seismic records obtained in instrumented buildings in California. *Proceedings of the 2017 Annual Meeting of the Los Angeles Tall Buildings Structural Design Council*, Los Angeles, 2017, pp. 65-80.

11. Xiang, Y., Harris, A., Naeim, F. and Zareian, F. Identification and validation of natural periods and modal damping ratios for seismic design and building code. *Proceedings of the*

2017 Annual Meeting of the Los Angeles Tall Buildings Structural Design Council, Los Angeles, 2017, pp. 81-95.

12. Task 7 Project Core Group of the PEER Tall Buildings Initiative. *Modeling and Acceptance Criteria for Seismic Design and Analysis of Tall Buildings*. Report No. PEER/ATC-72-1, Pacific Earthquake Engineering Research Center and Applied Technology Council, 2010.

13. Cruz, C. and Miranda, E. Evaluation of damping ratios for the seismic analysis of tall buildings. *Journal of Structural Engineering*, ASCE. Vol. 143, Issue 1, 2017.

14. Petrini, L., Maggi, C., Priestley, M.J.N. and Calvi, G.M. Experimental verification of viscous damping modeling for inelastic time history analyses. *Journal of Earthquake Engineering*. Vol. 12, sup1, 2008, pp. 125-145.

15. Correia, A.A., Almeida, J.P. and Pinho, R. Seismic energy dissipation in inelastic frames: understanding state-of-the-practice damping models. *Structural Engineering International*. Vol. 23, Issue 2, 2013, pp. 148-158.

16. Chrisp, D. J. *Damping Models for Inelastic Structures*. Department of Civil Engineering, University of Canterbury, Christchurch, New Zealand, 1980.

17. Bernal, D. Viscous damping in inelastic structural response. *Journal of Structural Engineering*, ASCE. Vol. 120, Issue 4, 1994, pp. 1240-1254.

18. Carr, A. J. Damping models for inelastic analyses. *Proceedings of the Asia-Pacific Vibration Conference*. Kyongju, Korea, 1997, pp. 42-48.

19. Carr, A. J. Damping models for time-history structural analysis. *Proceedings of the Asia-Pacific Vibration Conference*. Langkawi, Malaysia, 2005, pp. 287-293.

20. Hall, J. F. Problems encountered from the use (or misuse) of Rayleigh damping. *Earthquake Engineering and Structural Dynamics*. Vol. 35, Issue 5, 2006, pp. 525-545.

21. Carr, A. J. *Ruaumoko Volume 1: Theory*. Department of Civil Engineering, University of Canterbury, Christchurch, New Zealand, 2007.

22. Charney, F. Unintended consequences of modeling damping in structures. *Journal of Structural Engineering*, ASCE. Vol. 134, Issue 4, 2008, pp. 581-592.

23. Zareian, F. and Medina, R. A. A practical method for proper modeling of structural damping in inelastic plane structural systems. *Computers and Structures*. Vol. 88, Issues 1-2, 2010, pp. 45-53.

24. Chopra, A. K. and McKenna, F. Modeling viscous damping in nonlinear response history analysis of buildings for earthquake excitation. *Earthquake Engineering & Structural Dynamics*. Vol. 45, Issue 2, 2016, pp. 193-211.

25. Chopra, A. and McKenna, F. Response to John Hall's discussion (EQE-16-0008) to Chopra and McKenna's paper, 'Modeling viscous damping in nonlinear response history analysis of buildings for earthquake excitation.' *Earthquake Engineering & Structural Dynamics*. Vol. 45, Issue 13, 2016, pp. 2235-2238.

26. Luco, J. E. and Lanzi, A. A new inherent damping model for inelastic time-history analyses. *Earthquake Engineering and Structural Dynamics.* Vol. 46, Issue 12, 2017, pp. 1919-1939.

27. Wilson, E. L. and Penzien, J. Evaluation of orthogonal damping matrices. *International Journal for Numerical Methods in Engineering*. Vol. 4, Issue 1, 1972, pp. 5-10.

28. Caughey, T. K. and O'Kelly, M. E. J. Classical normal modes in damped linear dynamic systems. *Journal of Applied Mechanics*, ASME. Vol. 32, Issue 3, 1965, pp. 583-588.

29.. Hall, J. F. Seismic response of steel frame buildings to near-source ground motions. *Earthquake Engineering and Structural Dynamics*. Vol. 27, Issue 12, 1998, pp. 1445-1464.

30. Jehel, P., Léger, P. and Ibrahimbegovic, A. Initial versus tangent stiffness-based Rayleigh damping in inelastic time history seismic analyses. *Earthquake Engineering and Structural Dynamics*. Vol. 43, Issue 3, 2014, pp. 467-484.

31. Charney, F., Lopez-Garcia, D., Hardyniec, A. and Ugalde, D. Modeling inherent damping in nonlinear dynamic analysis. *Proceedings of the 16th World Conference on Earthquake Engineering*, Paper No. 181, Santiago, Chile, 2017.

32. Jehel, P. and Léger, P. Two types of spurious damping forces potentially modeled in numerical seismic nonlinear response history analysis. *Proceedings of the 16th World Conference on Earthquake Engineering*, Paper No. 3187, Santiago, Chile, 2017.

33. Medina, R. and Krawinkler, H. *Seismic Demands for Nondeteriorating Frame Structures and Their Dependence on Ground Motions*. Report No. PEER 2003/15, Pacific Earthquake Engineering Research Center, University of California, Berkeley, 2004.

34. Luco, J. E. and Lanzi, A. Optimal Caughey series representation of classical damping matrices. *Soil Dynamics and Earthquake Engineering*. Vol. 92, January 2017, pp. 253-265.

35. Leger, P. and Dussault, S. Seismic-energy dissipation in MDOF structures. *Journal of Structural Engineering*, ASCE. Vol. 118, Issue 5, 1992, pp. 1251-1269.

36. Priestley, M. J. N. and Grant, D. N. Viscous Damping in Seismic Design and Analysis. *Journal of Earthquake Engineering*. Vol. 9, Special Issue 2, 2005, pp. 229-255.

37. Hall, J.F. Discussion of "A new inherent damping model for inelastic time-history analyses" by Enrique Luco and Armando Lanzi. *Earthquake Engineering and Structural Dynamics*. Vol. 47, Issue 10, 2018, pp. 2137-2139.

38. Otani, S. Nonlinear dynamic analysis of reinforced concrete building structures. *Canadian Journal of Civil Engineering*. Vol. 7, No. 2, 1980, pp. 333-344.

39. Krawinkler, H. *State of the Art Report on Systems Performance of Steel Moment Frames Subject to Earthquake Ground Shaking*. Report No. FEMA-355C, Federal Emergency Management Agency, Washington, D. C., 2000.

40. Somerville, P., Smith, N., Punyamurthula, S. and Sun, J. *Development of Ground Motion Time Histories for Phase 2 of the FEMA/SAC Steel Project*. Report No. SAC/BD-97/04, SAC Joint Venture, 1997.

41. Tompkins, D. N. *The Seismic Response of Reinforced Concrete Multistorey Frames*. Department of Civil Engineering, University of Canterbury, Christchurch, New Zealand, 1980.

42. Clough, R.W. and J. Penzien. *Dynamics of Structures*, 2nd edition. McGraw-Hill, Inc., New York, New York, 1993.

43. Erduran, E. Evaluation of Rayleigh damping and its influence on engineering demand parameter estimates. *Earthquake Engineering & Structural Dynamics*. Vol. 41, Issue 14, 2012, pp. 1905-1919.

44. Papazoglou, A. J. and Elnashai, A. S. Analytical and field evidence of the damaging effect of vertical earthquake ground motion. *Earthquake Engineering & Structural Dynamics*. Vol. 25, Issue 10, 1996, pp. 1109-1137.

45. Harrington, C. C. and Liel, A. B. Collapse assessment of moment frame buildings, considering vertical ground shaking. *Earthquake Engineering & Structural Dynamics*. Vol. 45, Issue 15, 2016, pp. 2475-2493.

46. NEHRP Consultants Joint Venture. *Soil-Structure Interaction for Building Structures*. Report No. NIST GCR 12-917-21, National Institute of Standards and Technology, Gaithersburg, Maryland, 2012.

47. Cruz, C. and Miranda, E. Evaluation of soil-structure interaction effects on the damping ratios of buildings subjected to earthquakes. *Soil Dynamics and Earthquake Engineering*. Vol. 100, September 2017, pp 183-195.

48. Vrettos, C. Vertical and rocking impedances for rigid rectangular foundations on soils with bounded non-homogeneity. *Earthquake Engineering & Structural Dynamics*. Vol. 28, Issue 12, 1999, pp. 1525-1540.

49. Hall, J.F. and Challa, V.R.M. Beam-column modeling. *Journal of Engineering Mechanics*, ASCE. Vol. 121, Issue 12, 1995, pp. 1284-1291.

50. Lignos, D.G. and Krawinkler, H. Deterioration modeling of steel components in support of collapse prediction of steel moment frames under earthquake loading. *Journal of Structural Engineering*, ASCE. Vol. 137, Issue 11, 2011, pp. 1291-1302.

51. Challa, V.R.M. and Hall, J.F. Earthquake collapse analysis of steel frames. *Earthquake Engineering and Structural Dynamics*. Vol 23, Issue 11, 1994, pp. 1199-1218.

52. Huang, Y., Sturt, R and Willford, M. A damping model for nonlinear dynamic analysis providing uniform damping over a frequency range. *Computers and Structures*. Vol. 212, 2019, pp. 101-109.

12. FIGURES

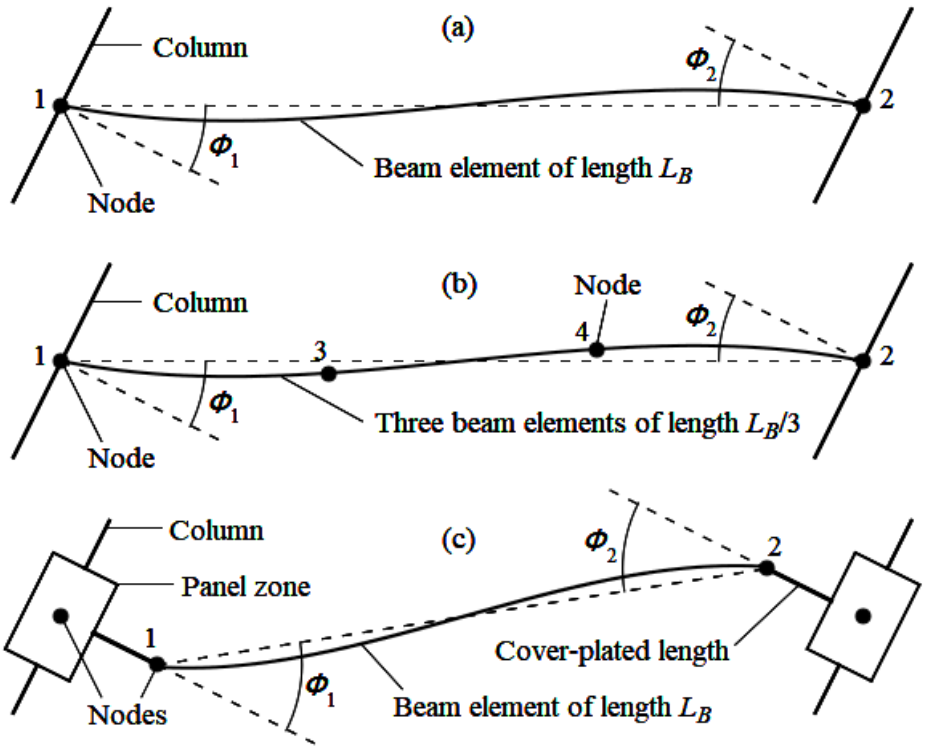

Figure 1. Three representations of a beam in a moment frame with implicit plastic hinges at the ends: (a) single beam element, (b) three-element model with third-point nodes and (c) single beam element with reduced span. Beam plastic hinges form at nodes 1 and 2, and L_B is the distance between these two nodes.

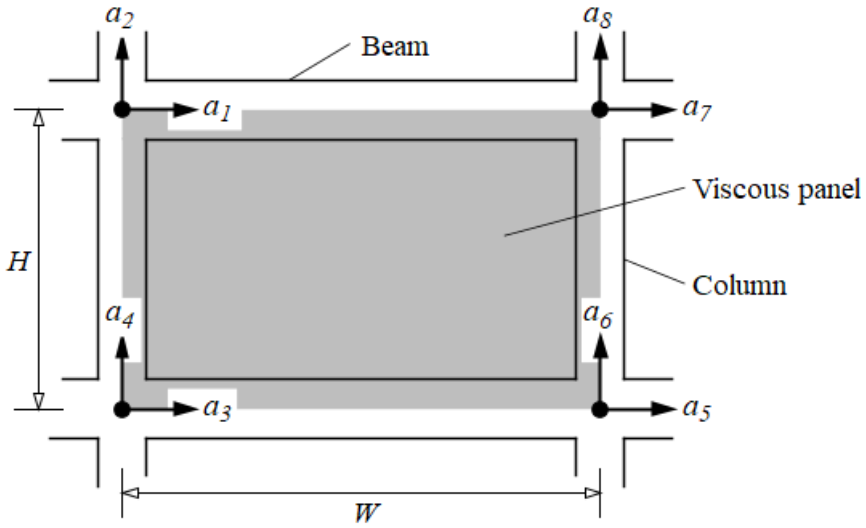

Figure 2. Rectangular viscous element showing position in a frame and numbering of the degrees of freedom. The panel has 4 nodes and 8 degrees of freedom.

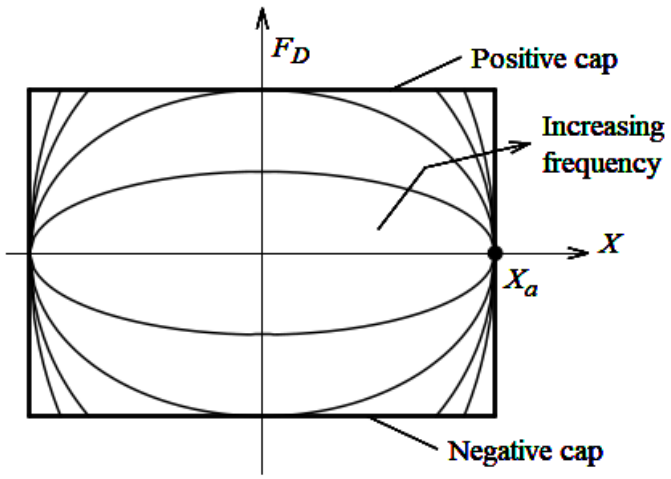

Figure 3. Damping force $F_D(t)$ vs displacement $X(t)$ for a capped viscous damper under harmonic motion with increasing frequency at constant displacement amplitude X_a.

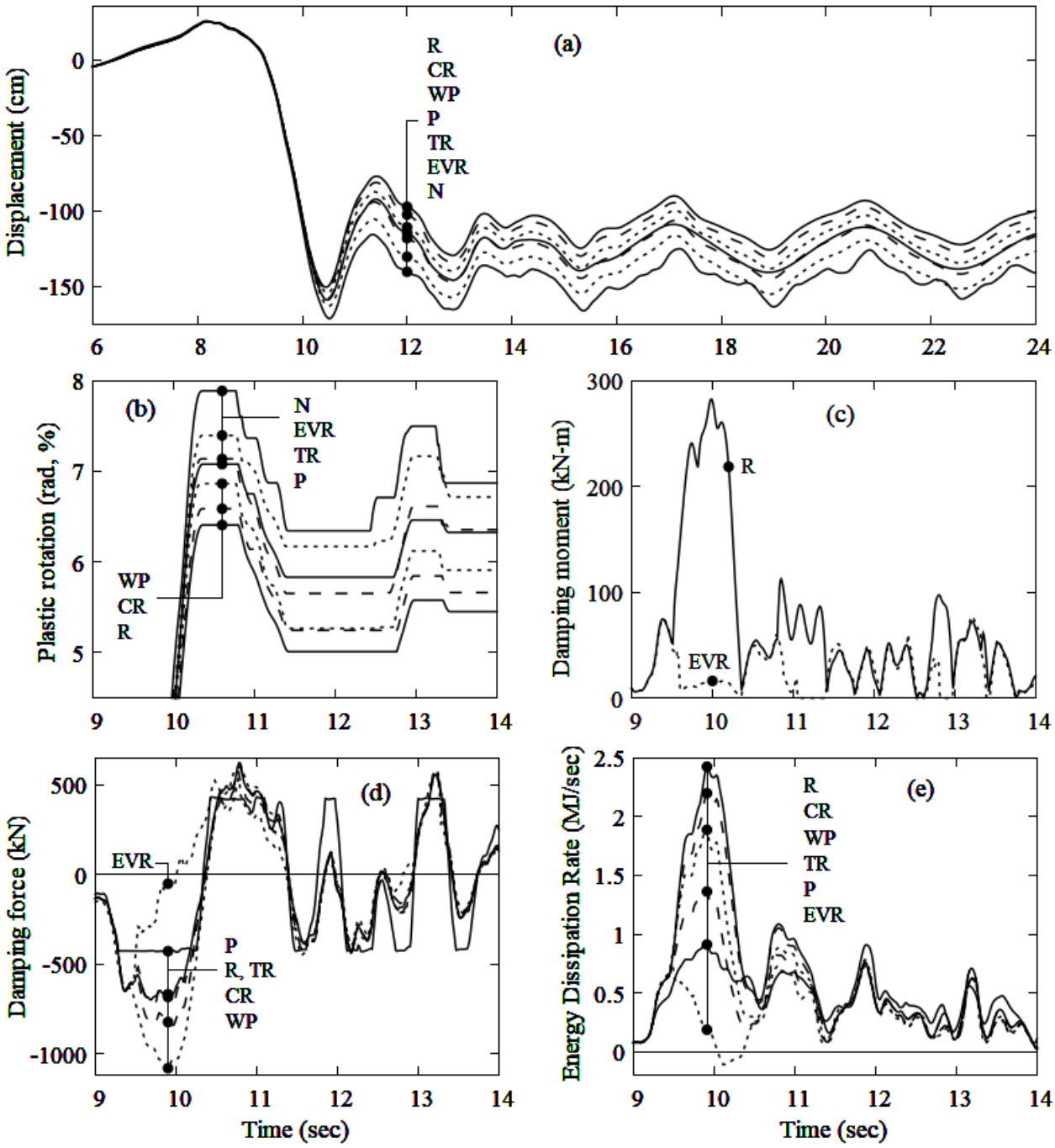

Figure 4. Time history plots for the 20-story building subjected to the LA35/LA36 ground motion scaled amplitude wise by $F = 0.50$: (a) 12th-floor lateral displacement, (b and c) maximum absolute value of the plastic hinge rotation and damping moment among all 5th-floor beams, (d) 4th-story damping force, and (e) rate of energy dissipation by damping.

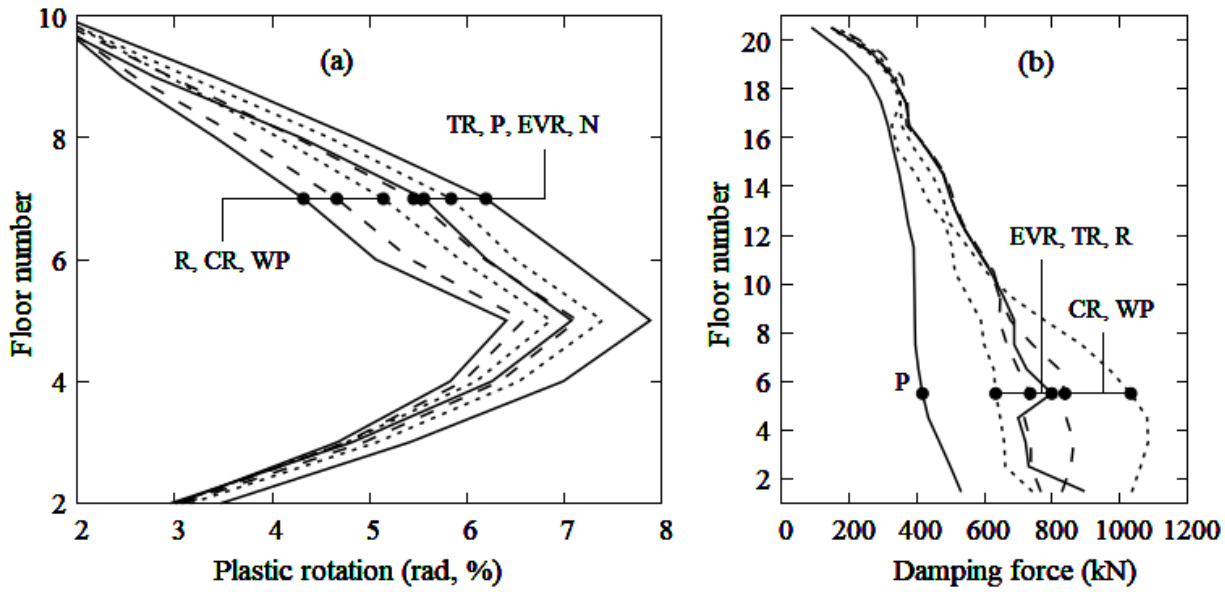

Figure 5. Distributions over the height for the 20-story building subjected to the LA35/LA36 ground motion scaled amplitude wise by $F = 0.50$: (a) peak plastic hinge rotation among the beams on each floor and (b) peak damping force in each story .

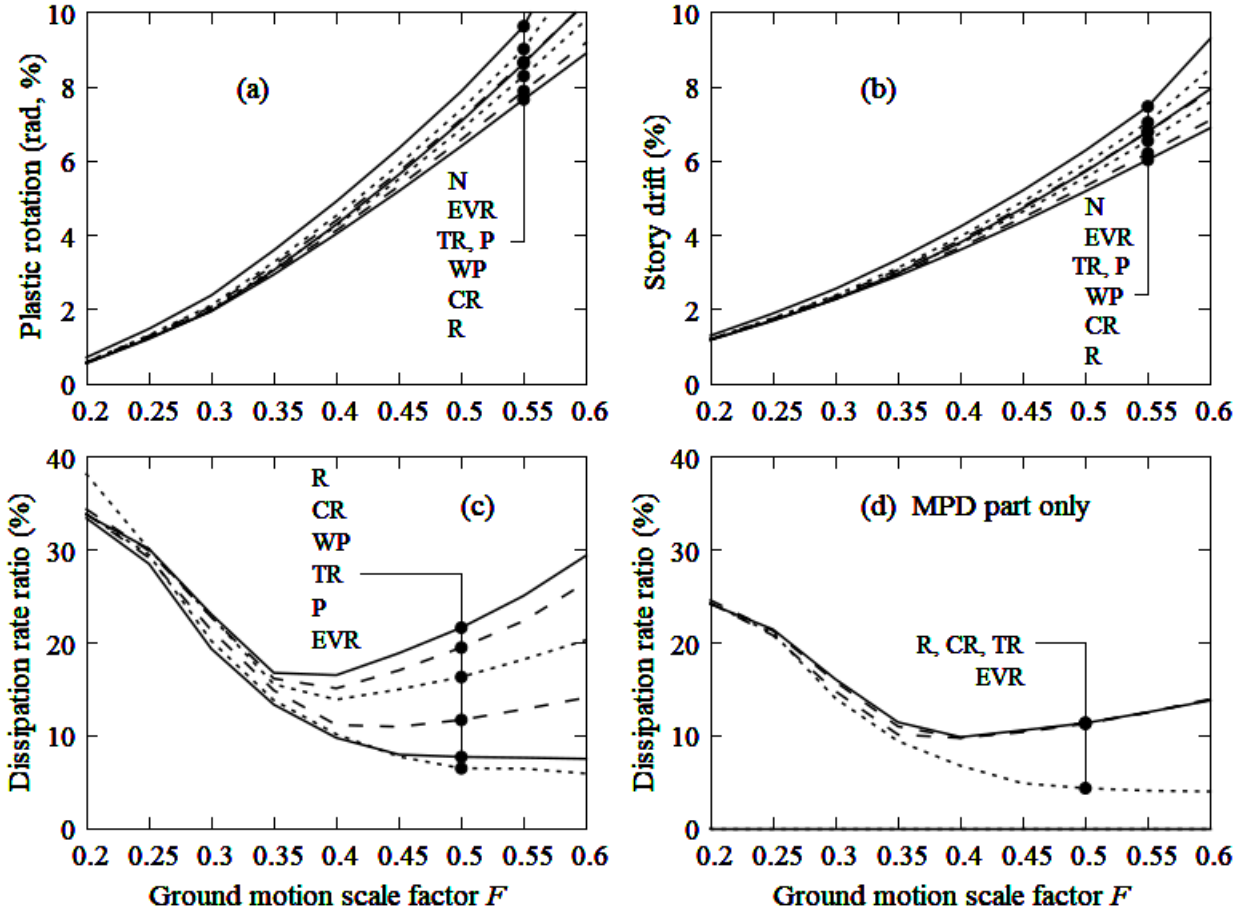

Figure 6. Variations in four quantities for the 20-story building as a function of the scale factor F for the LA35/LA36 ground motion varied from 0.20 to 0.60 in increments of 0.05: (a) peak plastic hinge rotation in any beam, (b) peak drift in any story, (c) ratio of peak rate of energy dissipation by damping to the peak rate of energy dissipation by hysteresis of the structural members, and (d) the same energy dissipation rate ratio but only including the mass proportional damping term.

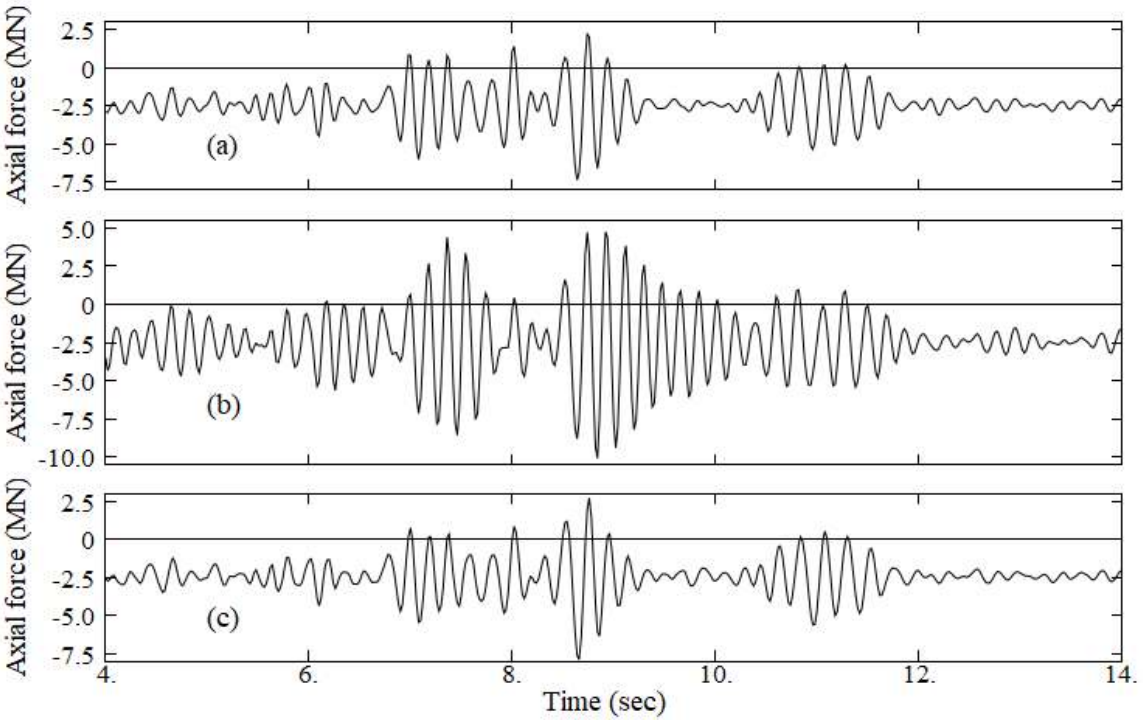

Figure 7. Column axial force time histories for the 20-story building due to the vertical component of the Tarzana ground motion (interior moment-frame column in the 2nd story): (a) Rayleigh damping with $\hat{\xi} = 0.03$ at $\hat{T}_1$ =4.0 sec and $\hat{T}_2$ =1.0 sec, (b) Rayleigh damping with $\hat{\xi} = 0.03$ at $\hat{T}_1$ =0.3 sec and $\hat{T}_2$ =0.1 sec, and (c) Rayleigh damping with $\hat{\xi} = 0.03$ at $\hat{T}_1$ =0.3 sec and $\hat{T}_2$ =0.1 sec and soil-structure interaction is included.

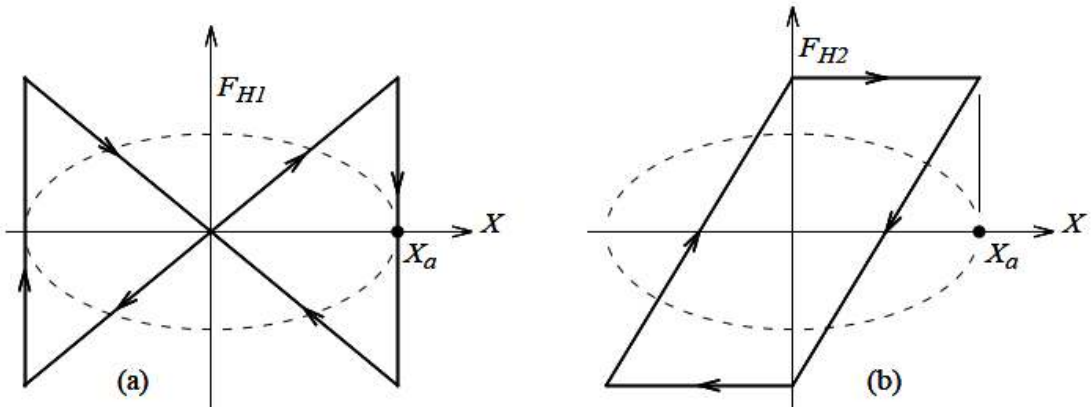

Figure A1. Force $F_H(t)$ vs displacement $X(t)$ for two types of hysteretic dampers: (a) force proportional to displacement and opposing velocity and (b) elastic-perfectly plastic. The dotted line in each part represents the force vs. displacement relation for a viscous damper under harmonic motion, and the plots are scaled such that the hysteretic and viscous dampers dissipate the same amount of energy per cycle under equal displacement amplitudes X_a.

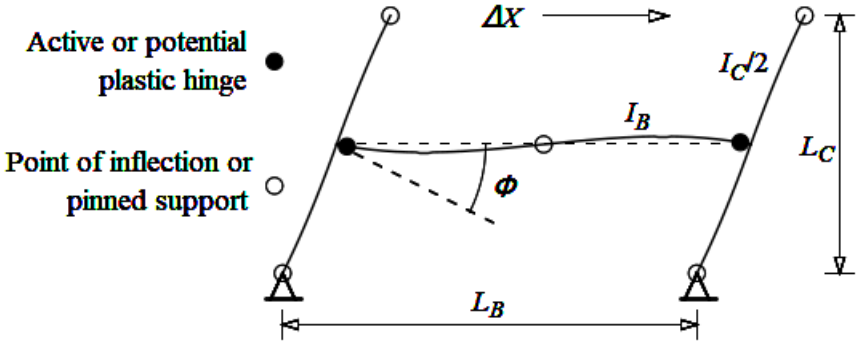

Figure A2. Partial moment frame used to demonstrate speed-up in joint rotations after plastic hinging occurs in the beam. One node is present at each beam-to-column joint. Finite joint dimensions are not included.

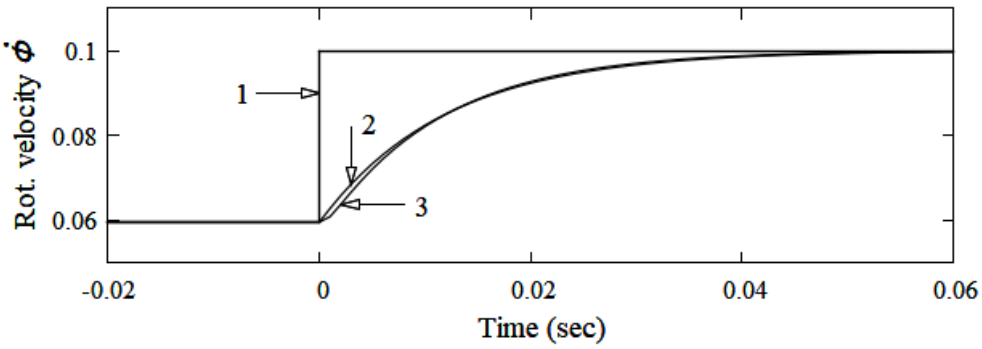

Figure A3. Nodal rotational velocity vs. time for the partial moment frame of Figure A2. Curve 1: neither damping nor rotational mass included. Curve 2: damping included but not rotational mass. Curve 3: both damping and rotational mass included. Hinge formation occurs at time zero. See the text for the parameters of the analysis.

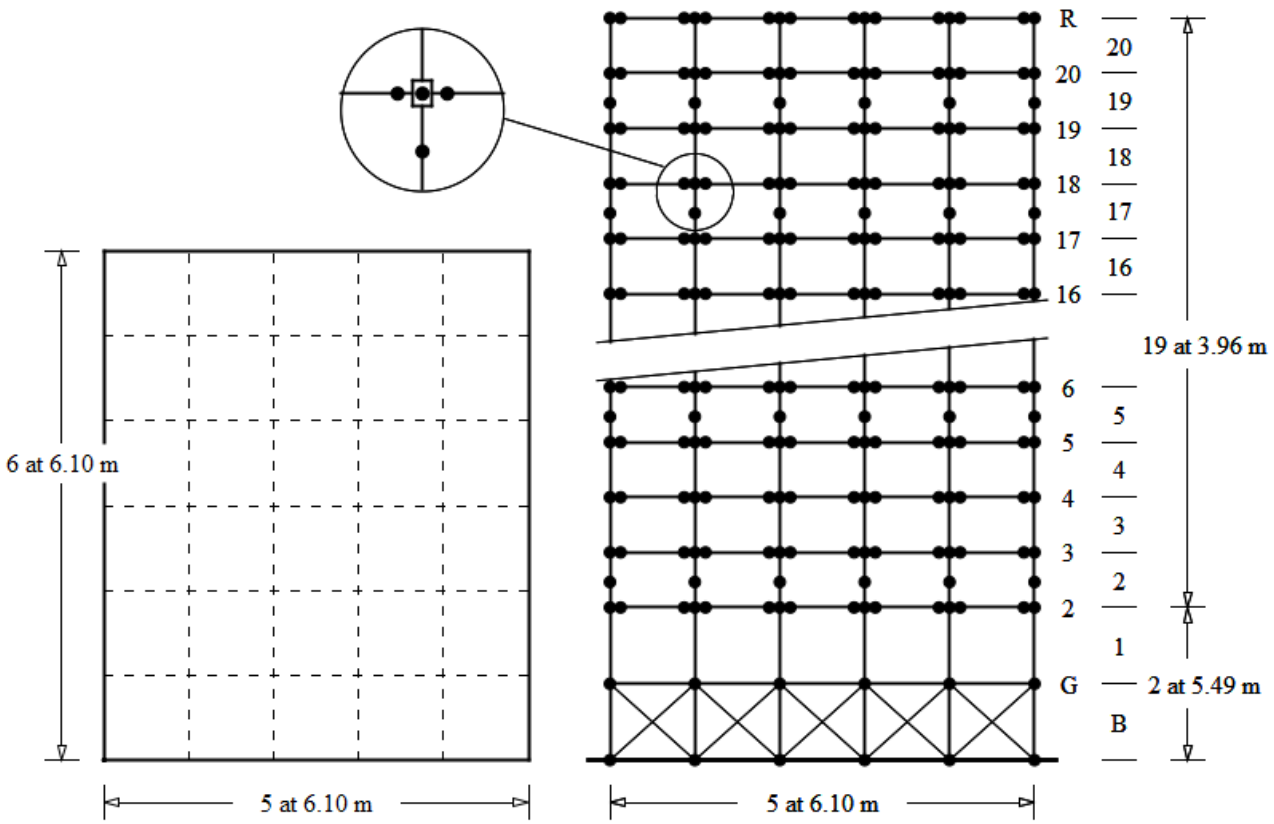

Figure A4. Plan view (left) and moment frame (right, displaying nodal layout) of the building analyzed. The enlargement shows panel zone with joint node, beam nodes at ends of cover-plated sections, and column-splice node. The gravity frame is similar except cover plates and the associated interior beam nodes are not present.

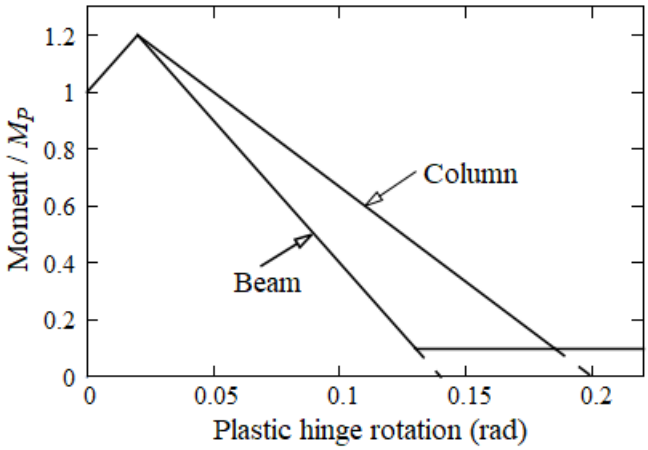

Figure A5. Moment vs. rotation relation for the plastic hinges, showing variable strength hinges for beams and columns.

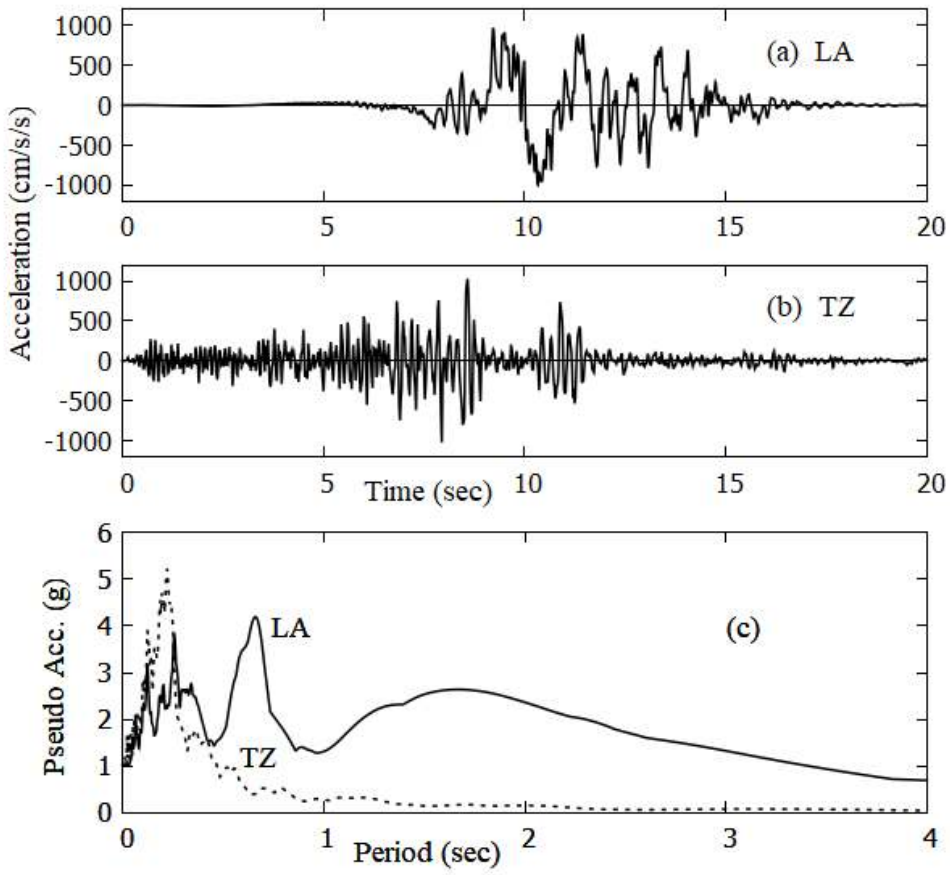

Figure A6. Acceleration time histories and pseudo acceleration response spectra for two ground motions: combined horizontal LA35 and LA36 from the SAC project (LA) and the vertical component from Tarzana recorded during the 1994 Northridge earthquake (TZ). Response spectra are computed with 3% damping.

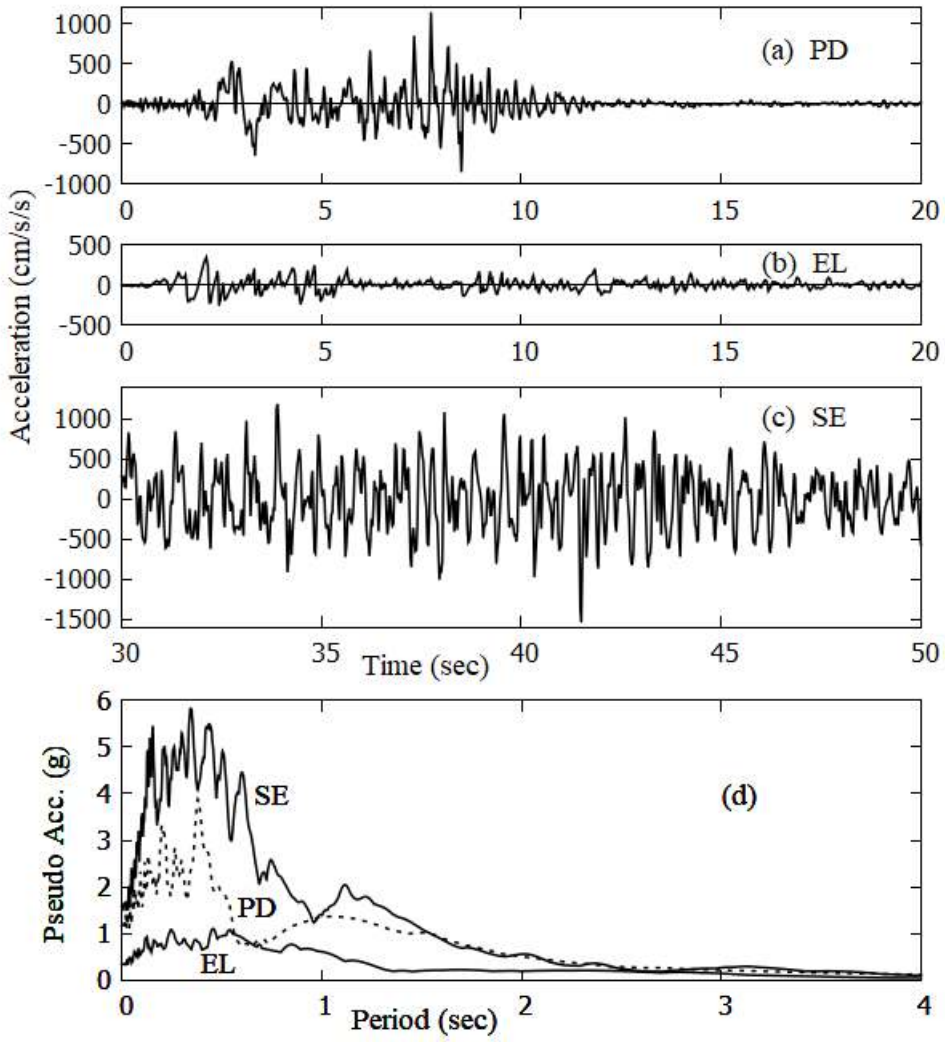

Figure A7. Acceleration time histories and pseudo acceleration response spectra for three ground motions: horizontal component S16E at Pacoima Dam recorded during the 1971 San Fernando earthquake (PD), horizontal component S00E in El Centro recorded during the 1940 Imperial Valley earthquake (EL), and horizontal SE30 from the SAC project (SE). Response spectra are computed with 3% damping.

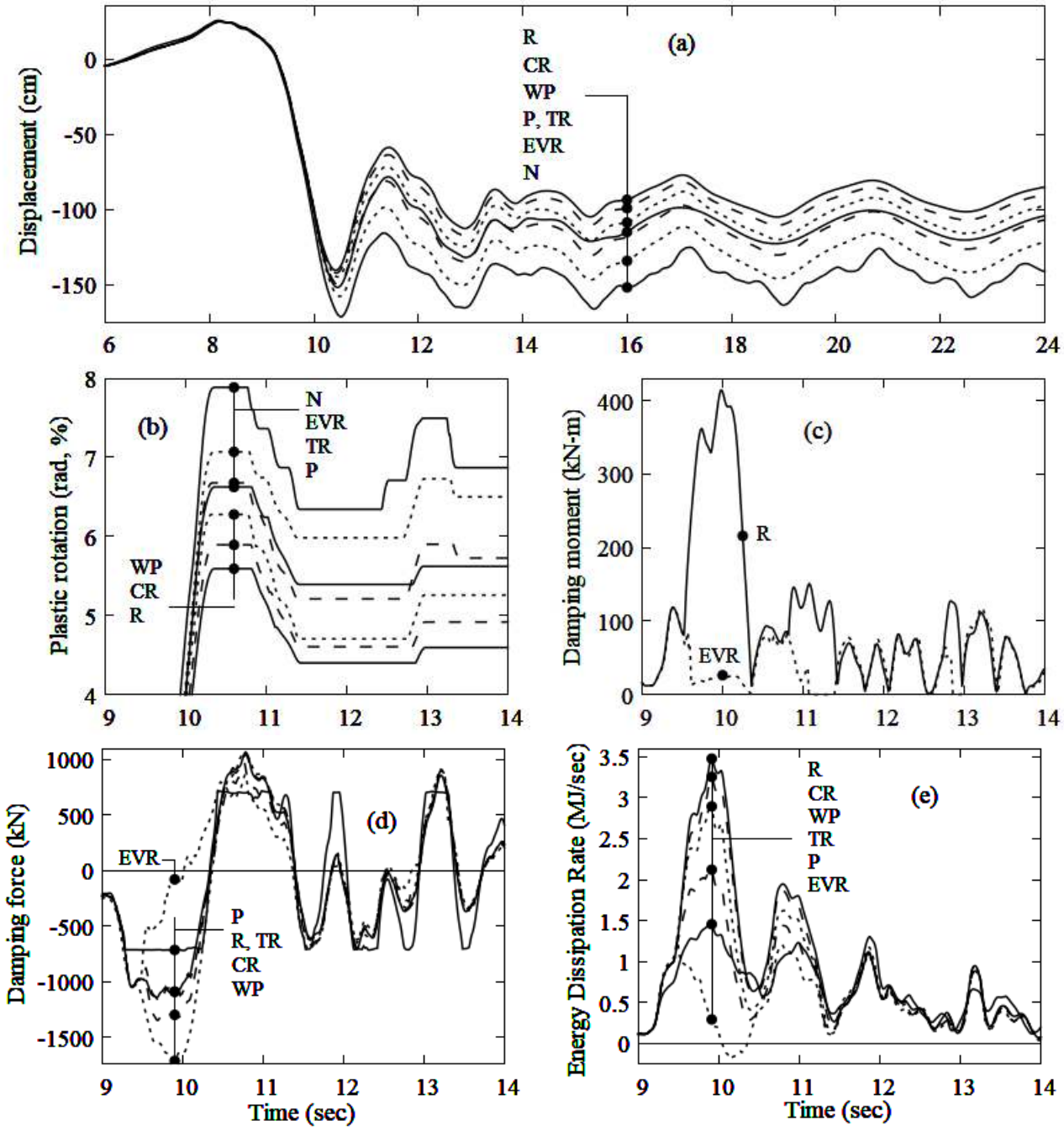

Figure A8. Time history plots for the 20-story building subjected to the LA35/LA36 ground motion scaled amplitude wise by $F = 0.50$: (a) 12th-floor lateral displacement, (b and c) maximum absolute value of the plastic hinge rotation and damping moment among all 5th-floor beams, (d) 4th-story damping force, and (e) rate of energy dissipation by damping. Same as Figure 4 except damping is increased to $\hat{\xi} = 0.05$.

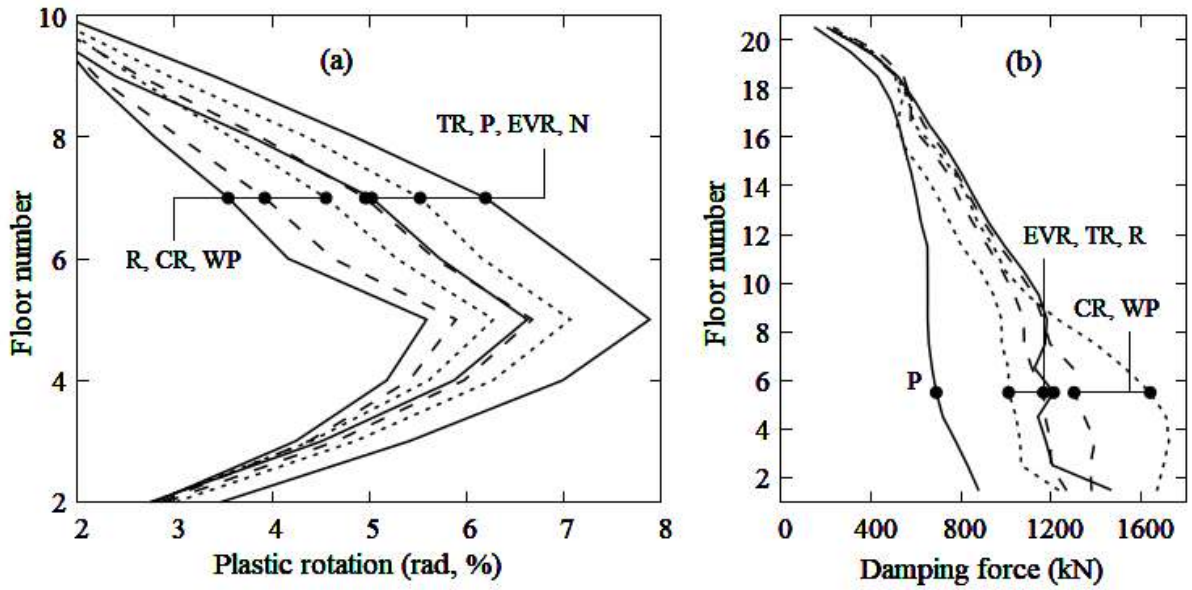

Figure A9. Distributions over the height of the 20-story building subjected to the LA35/LA36 ground motion scaled amplitude wise by $F = 0.50$: (a) peak plastic hinge rotation among the beams on each floor and (b) peak damping force in each story. Same as Figure 5 except damping is increased to $\hat{\xi} = 0.05$.

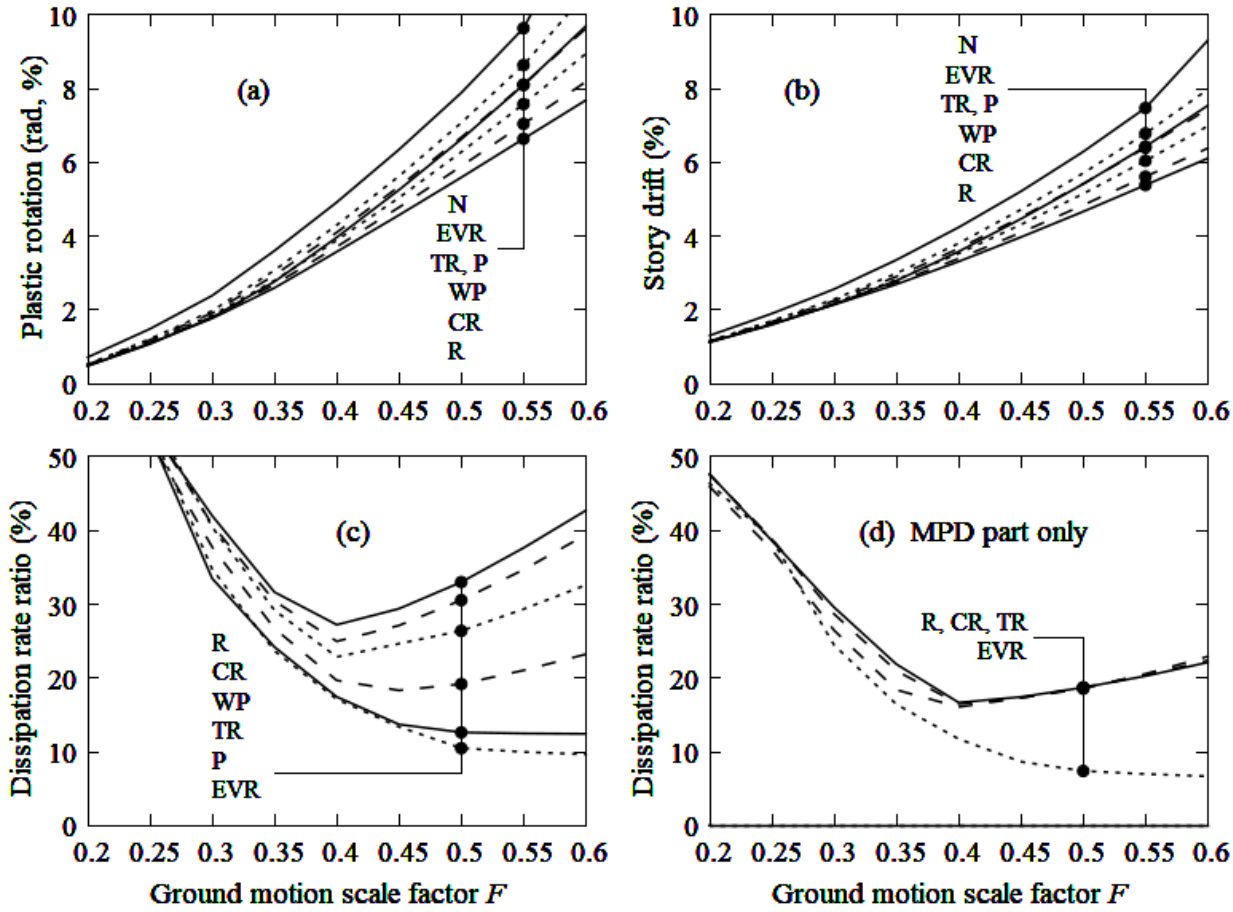

Figure A10. Variations in four quantities for the 20-story building as a function of the scale factor F for the LA35/LA36 ground motion varied from 0.20 to 0.60 in increments of 0.05: (a) peak plastic hinge rotation in any beam, (b) peak drift in any story, (c) ratio of peak rate of energy dissipation by damping to the peak rate of energy dissipation by hysteresis of the structural members, and (d) the same energy dissipation rate ratio but only including the mass proportional damping term. Same as Figure 6 except damping is increased to $\hat{\xi} = 0.05$.

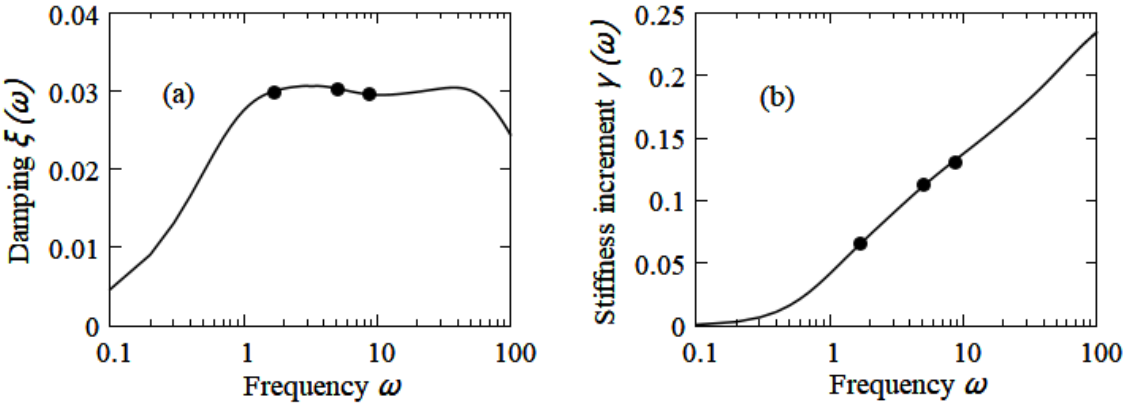

Figure A11. Damping $\xi(\omega)$ (part a) and stiffness increment $\gamma(\omega)$ (part b) for Arup damping at $\hat{\xi}$ = 0.03. Cutoff frequencies are 1, 4, 16 and 64 rad/sec. The dots are at the three lowest modal frequencies of the 20-story building (1.74, 5.1 and 8.8 rad/sec). (This figure is similar to one in Reference 52.)

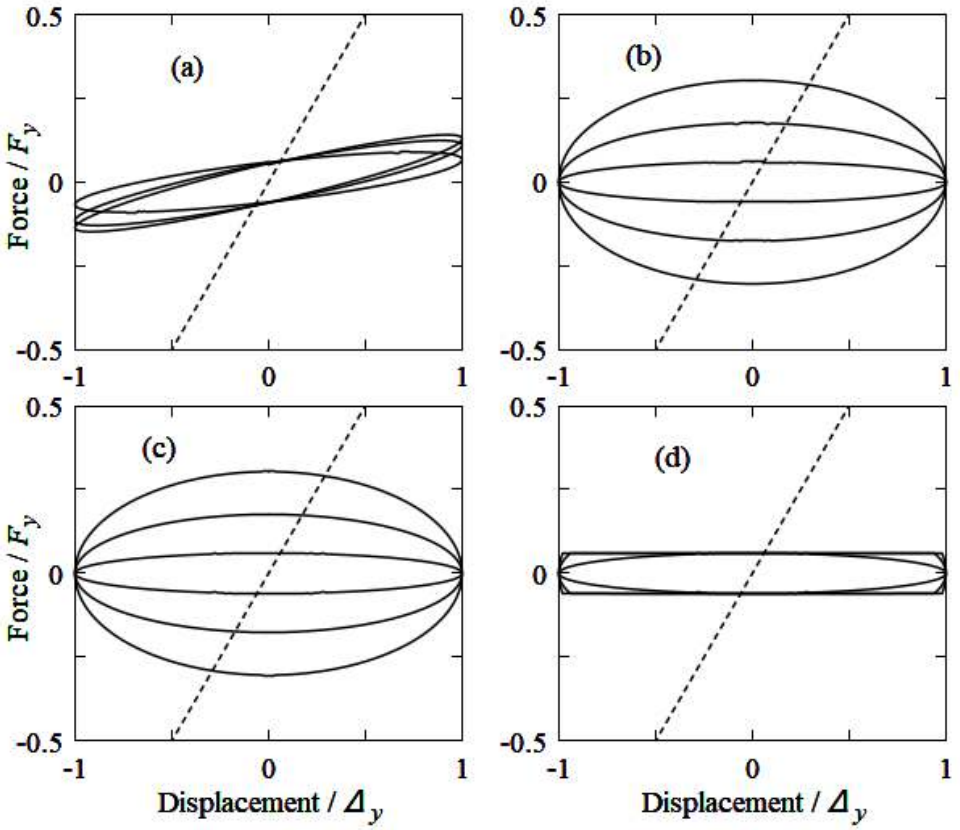

Figure A12. Spring force (dashed line) and damper force (solid lines) vs. displacement for a single degree of freedom oscillator subjected to a sinusoidal displacement at the yield displacement. Four damping cases are shown: Arup damping (part a), Rayleigh (part b), tangent Rayleigh (part c) and capped damping (part d). The damper force curves correspond to frequencies of 1.74 rad/sec (inner loop), 5.1 rad/sec (middle loop) and 8.8 rad/sec (outer loop).

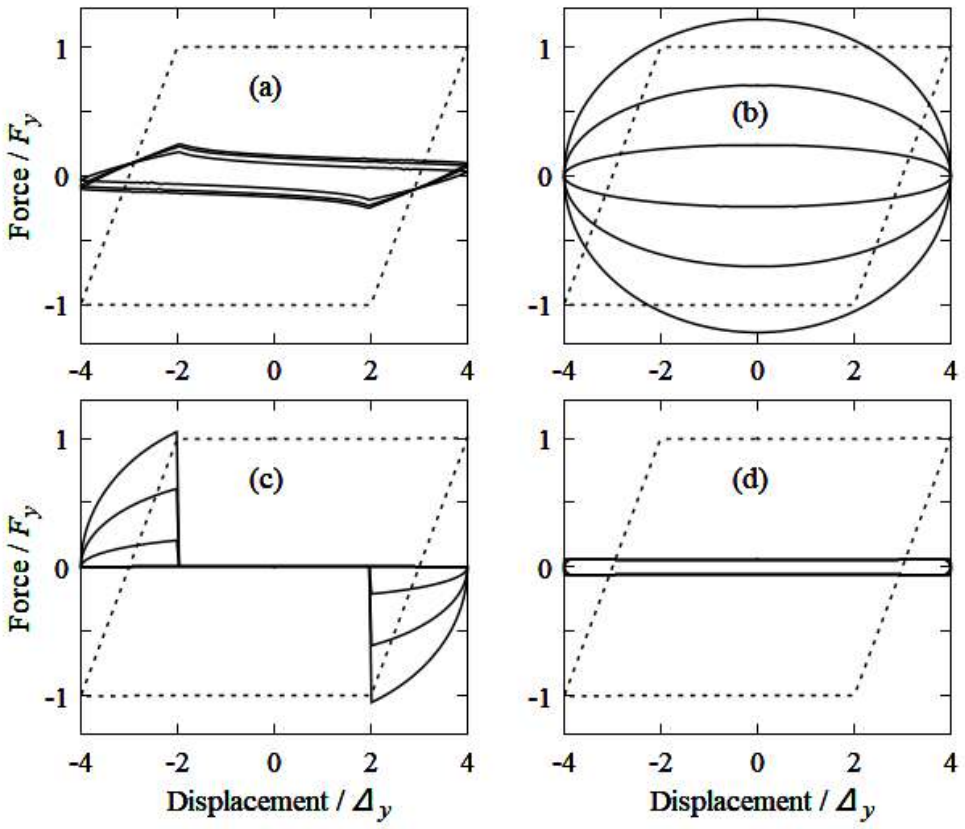

Figure A13. Spring force (dashed line) and damper force (solid lines) vs. displacement for a single degree of freedom oscillator subjected to a sinusoidal displacement at four times the yield displacement. Four damping cases are shown: Arup damping (part a), Rayleigh (part b), tangent Rayleigh (part c) and capped damping (part d). The damper force curves correspond to frequencies of 1.74 rad/sec (inner loop), 5.1 rad/sec (middle loop) and 8.8 rad/sec (outer loop).

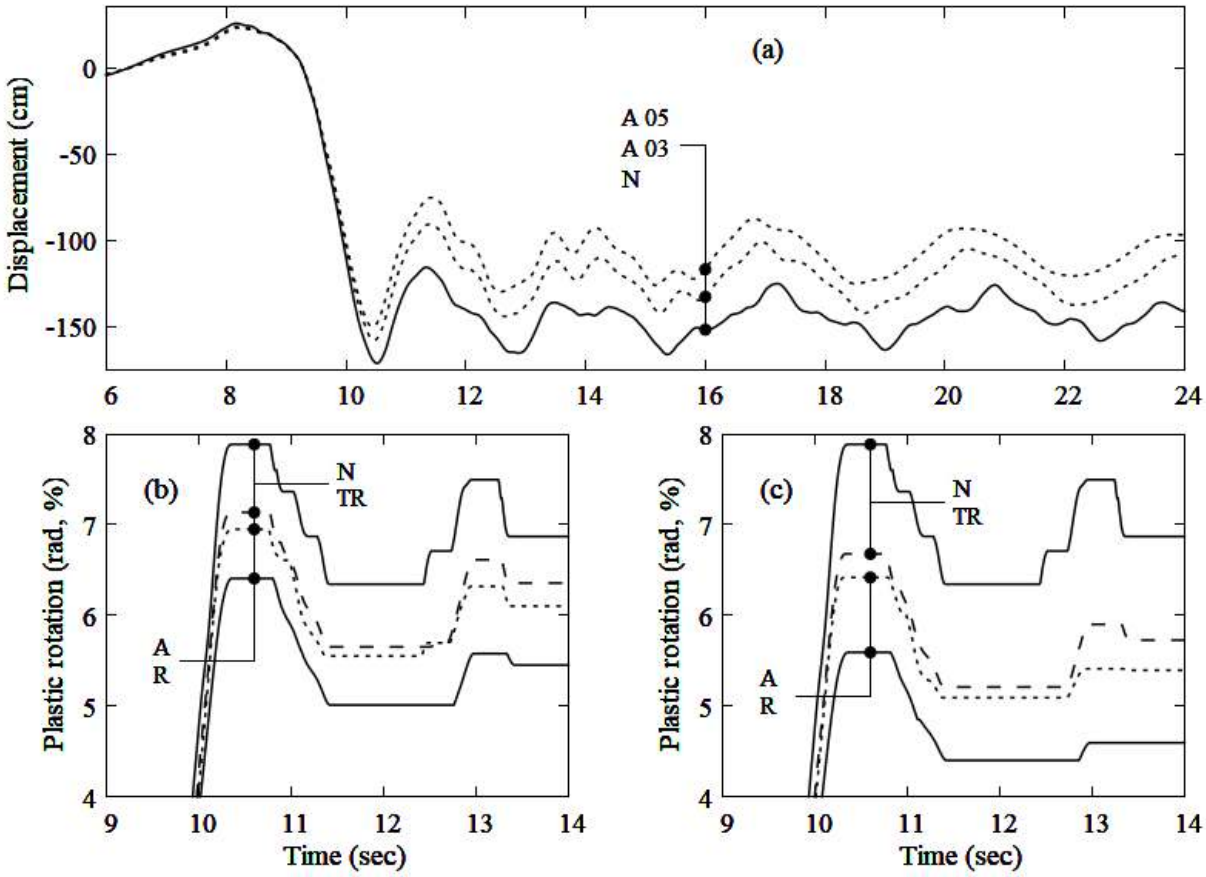

Figure A14. Time history plots for the 20-story building subjected to the LA35/LA36 ground motion scaled amplitude wise by $F = 0.50$: (a) 12th-floor lateral displacement and (b and c) maximum absolute value of the plastic hinge rotation among all 5th-floor beams. Damping is as noted for part a, $\hat{\xi} = 0.03$ for part b, and $\hat{\xi} = 0.05$ for part c.

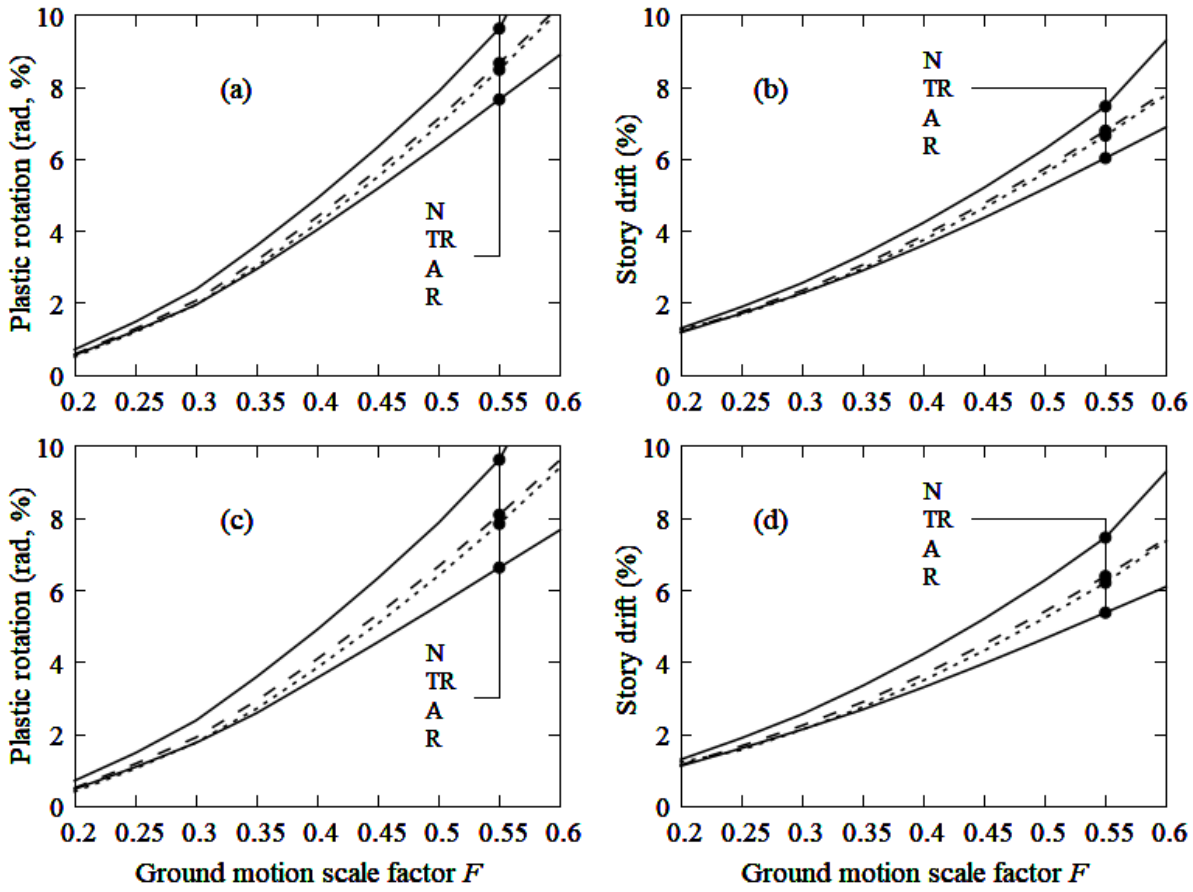

Figure A15. Variations in two quantities for the 20-story building as a function of the scale factor F for the LA35/LA36 ground motion varied from 0.20 to 0.60 in increments of 0.05: (a and c) peak plastic hinge rotation in any beam and (b and d) peak drift in any story. $\hat{\xi} = 0.03$ for parts a and b, and $\hat{\xi} = 0.05$ for parts c and d.